MOX–Report No. 37/2014

FEM SUPG stabilisation of mixed isoparametric BEMs: application to linearised free surface flows

Giuliani, N.; Mola, A.; Heltai, L.; Formaggia,L.

MOX, Dipartimento di Matematica "F. Brioschi"
Politecnico di Milano, Via Bonardi 9 - 20133 Milano (Italy)

mox@mate.polimi.it http://mox.polimi.it

FEM SUPG stabilisation of mixed isoparametric BEMs: application to linearised free surface flows

Nicola Giuliani Andrea Mola Luca Heltai
Luca Formaggia

May 31, 2014

Abstract

In finite element formulations, transport dominated problems are often stabilised through the Streamline-Upwind-Petrov-Galerkin(SUPG) method. Its application is straightforward when the problem at hand is solved using Galerkin methods. Applications of boundary integral formulations often resort to collocation techniques which are computationally more tractable. In this framework, the Galerkin method and the stabilisation may still be used to successfully apply boundary conditions and resolve instabilities that are frequently observed in transport dominated problems.

We apply this technique to an adaptive collocation boundary element method for the solution of stationary potential flows, where we solve a mixed Poisson problem in boundary integral form, with the addition of linearised free surface boundary conditions. We use a mixed boundary element formulation to allow for different finite dimensional spaces describing the flow potential and its normal derivative, and we validate our method simulating the flow around both a submerged body and a surface piercing body.

The coupling of mixed surface finite elements and strongly consistent stabilisation techniques with boundary elements opens up the possibility to use non conformal unstructured grids with local refinement, without introducing the inconsistencies of other stabilisation techniques based on up-winding and finite difference schemes.

Keywords: linearised free surface, submerged spheroid, Wigley hull, local refinement, SUPG, BEM, high order elements, FEM BEM coupling

Contents

1 Introduction

Given the constant increase of computing power, numerical simulations based on mathematic models are nowadays becoming a growingly important tool for ship performance prediction. In particular, models based upon the potential flow theory are very often used in the early stages of ship design, as they are particulary suitable for a quick estimation of the drag component resulting from the wave generation of a ship hull advancing on the water surface. If the fluid is assumed incompressible and the flow irrotational, Navier–Stokes equation can be simplified into Laplace and Bernoulli equations. Despite the presence of a linear differential operator, the equations have to be solved in the moving and *a-priori* unknown

domain representing the portion of water surrounding the hull, producing a non-linear boundary value problem. Such a problem is typically discretised by means of a Mixed Eulerian–Lagrangian approach, which consists in splitting each time step into an Eulerian and a Lagrangian sub-step. In the Eulerian sub-step, the potential field equations are solved to obtain the fluid velocities. The flow field obtained is then used in the Lagrangian sub-step to displace in a Lagrangian way the free-surface, and compute the corresponding potential field values [25]. In the most common practice, a boundary integral formulation is used to tackle the boundary value problem for the free surface flow potential. In this framework, Green's second identity is used to reformulate the original Laplace Equation for the flow potential into a Boundary Integral Equation (BIE). As the BIE only involves points on the domain boundaries, it is discretised by means of a Boundary Element Method (BEM), in which the computational grid needs to be generated only on the boundaries. The application of BEM to ship wave drag prediction is well documented in naval architecture [10, 17, 18, 23, 29].

Under the condition that only small waves are created (i.e., if we consider the wave amplitude A and its wavelength λ we have that $A \ll \lambda$), it is possible to apply a perturbation analysis to the fully nonlinear free surface boundary conditions, to obtain a linearised free surface boundary condition for the flow potential [21, 14]. The importance of such linearised condition lies in the fact that in the linear case it is possible to exploit the superposition principle to separately evaluate the flow fields related to diffraction and radiation. In addition, since the linearised condition is imposed on the undisturbed free surface, the computational grid does not need to be deformed during the simulations, leading to an enormous computational advantage with respect to the fully non-linear case. Yet, as pointed out in [24], the linearisation process leads to a symmetric condition in the stream wise direction which can possibly lead to unphysical results in presence of a main stream. It is well known in fact, that the waves generated by the motion of the body propagate mostly downstream, originating the so called Kelvin wake pattern.

For these reasons, several methods have been developed for the solution of the linearised free surface potential problem. Among others, in [20] and [22], the authors studied the possibility to employ *ad hoc* Green functions, called Kelvin sources, which automatically satisfy the linearised condition and suppress unphysical waves propagating upstream. Although this approach leads to good results, its numerical implementation is rather cumbersome. In particular, Kelvin sources are much more complex that the classic Rankine sources employed in standard BEM implementations. Further studies on the expression of such Green functions can be found in [8] and [15]). The behavior of such a Green function can in fact be highly oscillatory (as described in [7] and [27]) which can make even more difficult the —already critical— evaluation of the singular kernels in the BIE equation. A dif-

ferent strategy, proposed by Dawson in [10], consists in suppressing the undesired upstream waves at the numerical level, by employing an upwind finite difference approximation of the second order derivatives of the potential which appear in the linearised free surface boundary conditions.

In the numerical methodology proposed by Dawson the zeroth order term considered in the perturbation analysis expansion is the double body potential, which is obtained by imposing homogeneous boundary conditions at the undisturbed free surface. The free surface boundary condition (here linearised starting from the double body solution) is discretised with an upwind finite difference scheme once a structured grid is built exploiting the double body streamlines.

Dawson's method leads to accurate results with a simpler implementation with respect to Neumann–Kelvin method, however, it presents a two remarkable drawbacks: i) it requires the preliminary solution of an additional BEM problem to obtain the double body potential, and ii) the use of an upwind finite difference scheme requires the generation of a structured computational grid, where the nodes are aligned in the wind —or streamwise— direction. It is generally more difficult to generate these grids with respect to unstructured meshes, which can adapt more successfully to complex geometric configurations. Moreover, the upwind finite difference scheme is not easily compatible with a local adaptive refinement strategy.

In this work, we present a modification of Dawson's approach that allows the use of unstructured non conformal grids. The second order derivatives appearing in the linearised free surface boundary condition are here computed making use of a Streamline Upwind Petrov Galerkin (SUPG) stabilisation strategy [2]. In this framework, unphysical upstream waves are suppressed by the introduction of additional terms in the discretised formulation of the BIE. Such additional terms are independent of the grid employed, making it possible to use unstructured, non conformal grids.

SUPG is a common stabilisation method in the field of finite elements discretisation methods. To the best of the authors' knowledge, its application to the numerical solution of fully nonlinear potential free surface problems through BEM has been discussed for the first time in [17, 18]. This contribution describes the application of SUPG to the linearised free surface potential model. Thanks to the use of Telles' [26] quadrature rule for the integration of singular kernels, the methodology proposed allows for the use of arbitrary order boundary elements, and is even compatible with isogeometric discretisations [5]. Both linear and quadratic panels have been considered in this work, while the developement of an isogeometric solver is underway. The first test case considered is that of a fully submerged spheroid advancing at constant speed in calm water. The results of the numerical simulations are compared to analytic solutions proposed in [14] and to the nonlin-

ear simulations proposed in [24]. To test the free surface model for the case of a surface piercing body, the second test case considered is that of a Wigley hull advancing at constant speed in calm water. In this case, the results of the numerical simulations will be compared with experimental data [16] and numerical solutions obtained with different linear [23, 24] and nonlinear [18] potential models.

2 Free-Surface Flows

We are interested in studying the generation of gravitational waves around a body advancing at constant speed in calm water. This type of waves presents a typical pattern, called the Kelvin-wake pattern, which is characterised by a strongly V-shaped system. In section 4.1 we will focus on the waves generated by a fully submerged spheroid (Figure 1), while in section 4.2 we will study the waves generated by a surface piercing body (Figure 2). Both problems are assessed benchmarks in naval engineering (see, e.g., [21, 10, 23]).

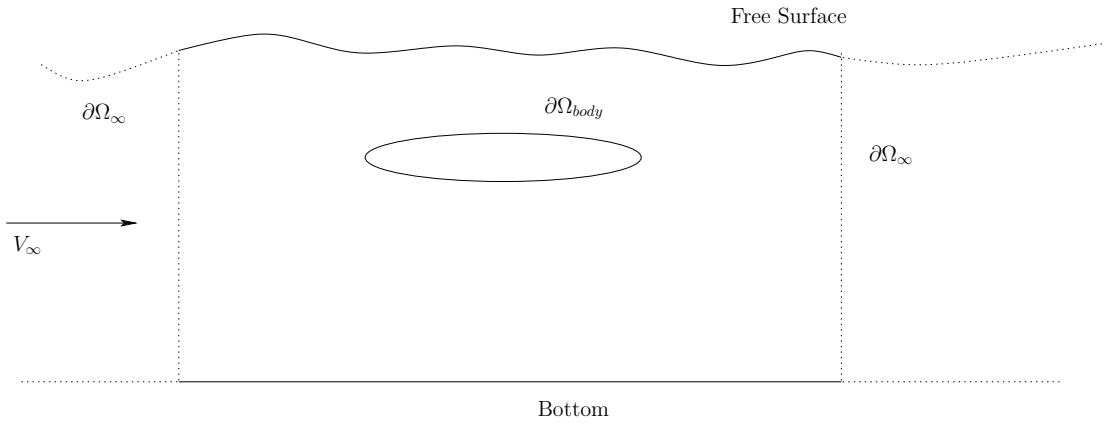

Figure 1: Vertical section of the domain for the simulation of the flow past a body beneath the water free surface.

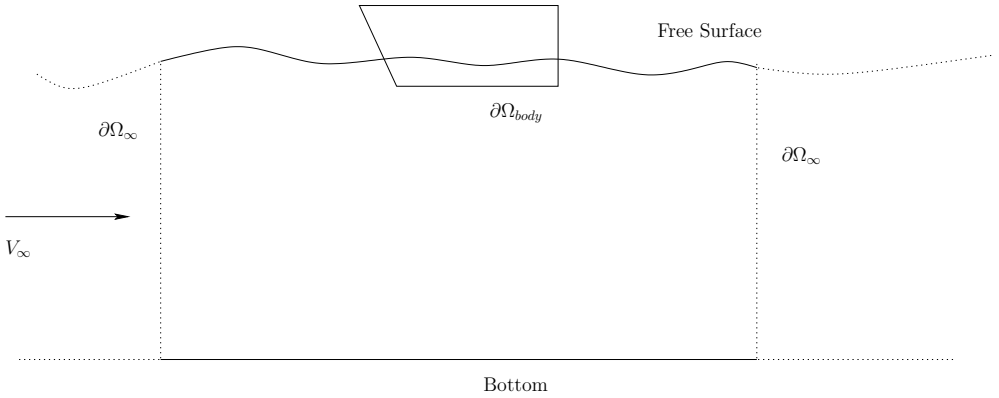

Figure 2: Vertical section of the domain for the simulation of the flow past a boat located across the water free surface

In all simulations we consider a flow domain composed by the portion of water surrounding the body, as depicted in Figures 1 or 2. The flow domain is bounded by the free surface, by the body and by the bottom surfaces. The part of the boundary Γ_∞ represents the truncation surfaces of the numerical domain, which is considered to be far enough from the body.

If the body pierces the free surface, as in Fig. 2, the domain includes only the part of the body beneath the water surface, excluding its dry part.

2.1 Governing equations inside the domain

We consider the flow of an incompressible inviscid fluid past a body at rest, or, equivalently, that of a body moving at constant speed in a fluid at rest, in a frame of reference attached to the body. If we neglect viscous forces, the governing equations reduce to the incompressible Euler equations of fluid dynamics:

$$\begin{cases} \dfrac{\partial}{\partial t}\mathbf{v} + (\mathbf{v}\cdot\nabla)\mathbf{v} = -\dfrac{1}{\rho}\nabla p + \mathbf{g} & \text{in } \Omega \\ \nabla\cdot\mathbf{v} = 0 & \text{in } \Omega \\ + \text{ initial and boundary conditions} \end{cases} \tag{1}$$

where ρ is the constant fluid density, $\mathbf{v}(\mathbf{x},t)$ is the fluid velocity, $p(\mathbf{x},t)$ is the pressure, and $\mathbf{g}$ is the gravity acceleration. We will drop the explicit dependence of velocity and pressure fields on the position vector $\mathbf{x} = (x,y,z) \in \Omega$ and on the time variable t. System (1) is closed when we supply initial and boundary conditions for the velocity field, as well as an evolution equation for the (moving) free surface.

We start by considering a decomposition for the velocity as

$$\mathbf{v} = \mathbf{v}_\infty + \mathbf{v}_\mathbf{p}, \tag{2}$$

where $\mathbf{v}_\infty \equiv (U_\infty, 0, 0)$ is a uniform background velocity field while $\mathbf{v_p}$ is the perturbation velocity field created by the body. In the chosen frame of reference the x axis is directed as $\mathbf{v}_\infty$, the z axis is vertical and pointing upwards, and the y axis is chosen consequently.

If the flow is assumed irrotational, *i.e.*, $\nabla \times \mathbf{v} = 0$ in Ω, the velocity can be represented as the gradient of a scalar function. Namely,

$$\mathbf{v} = \mathbf{v}_\infty + \mathbf{v_p} = \nabla\Phi = \mathbf{v}_\infty \cdot \mathbf{x} + \nabla\phi.$$

This assumption is consistent with the hypothesis of inviscid flow since, in absence of a viscous term, if the initial condition of undisturbed flow is irrotational, it must remain irrotational at all times. Under these assumptions, the conservation of mass, *i.e.* the second of equations (1) above, can be rewritten as a Laplace equation

$$\Delta\phi = 0, \tag{3}$$

while the balance of momentum, i.e. the first of equations (1), reduces to Bernoulli's equation, which expresses the pressure P as a function of the potential ϕ, namely

$$\frac{\partial\phi}{\partial t} + \frac{1}{2}\nabla\phi \cdot \nabla\phi + gz + \frac{P}{\rho} = C(t). \tag{4}$$

A consequence of the irrotational flow assumption is that the conservation of mass is decoupled from the momentum balance, and the two problems can be solved one after the other.

2.2 Free surface boundary conditions

We now briefly discuss the boundary condition to be imposed on the free surface following what is presented in [21]. We consider a main flow velocity $\mathbf{v}_\infty$ defined as $\mathbf{v}_\infty = U_\infty \mathbf{e}_x$ where $\mathbf{e}_x$ identifies the x axis of our domain. We assume, as in [18, 21], that it is possible to represent the free surface elevation as a Cartesian function (thus excluding breaking waves), in which the z coordinate is a single valued function of the horizontal coordinates x, y:

$$\sigma(x, y, z, t) = z - \eta(x, y, t) = 0. \tag{5}$$

By a kinematic stand point, one requires that fluid particles on the free surface will remain on the free surface, and fullfill equation (5). By a dynamical point of view instead, the water pressure on the free surface must always be equal to the air atmospheric pressure P_a, which is assumed constant and uniform. These two conditions can be expressed as

$$\frac{D}{Dt}(\sigma) = \frac{D}{Dt}(z - \eta) = 0 \tag{6}$$

and

$$\frac{\partial \Phi}{\partial t} + \frac{1}{2}\nabla\Phi \cdot \nabla\Phi + g\eta = C(t). \tag{7}$$

The first expression is the so-called kinematic boundary condition and it states that the material derivative of the quantity $z - \eta$ vanishes on the free surface boundary. The second, dynamic, condition is obtained from Bernoulli equation evaluated on the free surface. In the dynamic bernoulli equation, $C(t)$ is an arbitrary function of time, and can be fixed by imposing the atmospheric pressure and evaluating (7) at infinity, where the flow is assumed uniform, and both the perturbation potential ϕ, and the free surface elevation η vanish. We obtain

$$C(t) = \lim_{|\mathbf{x}|\to\infty} \left(\frac{\partial \Phi(\mathbf{x}, t)}{\partial t} + \frac{1}{2}\nabla\Phi(\mathbf{x}, t) \cdot \nabla\Phi(\mathbf{x}, t) + g\eta(x, y) \right) = \frac{1}{2}U_\infty^2. \tag{8}$$

A perturbation technique allows us to obtain a single, linearised, free surface boundary condition from equations (6) and (7). In equation (7) there are two unknown quantities, *i.e.*, Φ and η. We consider small perturbations of Φ and η, with respect to the undisturbed asymptotic flow given by $\Phi_0 = \mathbf{v}_\infty \cdot \mathbf{x}$ and $\eta_0 = 0$. The asymptotic expansions read

$$\Phi = \Phi_0 + \epsilon\Phi_1 + O(\epsilon^2) \tag{9}$$

$$\eta = \eta_0 + \epsilon\eta_1 + O(\epsilon^2). \tag{10}$$

Plugging these expansions into equation (6) and equating terms of order ϵ, we obtain

$$\frac{\partial \Phi_1}{\partial z} - \nabla\Phi_0 \cdot \nabla\eta_1 - \nabla\Phi_1 \cdot \nabla\eta_0 = 0, \tag{11}$$

$$\frac{\partial \Phi_1}{\partial t} + \nabla\Phi_0 \cdot \nabla\Phi_1 + g\eta_1 = 0. \tag{12}$$

We can write $\nabla\Phi_0 = \mathbf{v}_\infty$, $\phi = \epsilon\Phi_1$ and $\eta = \epsilon\eta_1$, leading to

$$\frac{\partial \phi}{\partial z} - \mathbf{v}_\infty \cdot \nabla\eta = 0, \tag{13}$$

$$\frac{\partial \phi}{\partial t} + \mathbf{v}_\infty \cdot \nabla\phi + g\eta = 0. \tag{14}$$

From equation (14) we see clearly that the imposition of the linearised boundary condition requires the resolution of a transport problem. This kind of problem often needs some kind of stabilisation. We will discuss this topic in section 3.3. If we consider the steady state solution and if we assume that $\mathbf{v}_\infty = \mathbf{e}_x U_\infty$, the two linearised equations can be combined together as

$$U_\infty^2 \frac{\partial^2 \phi}{\partial x^2} + g\frac{\partial \phi}{\partial z} = 0 \quad \text{at} \quad z = 0. \tag{15}$$

Following [21] we apply equation (15) to the perturbation potential ϕ. This is a reasonable approximation if we assume that only small waves are generated, i.e., if the wave amplitude A is much smaller than its wavelength λ ($A \ll \lambda$). If we exploit the fact that the undisturbed free surface is flat, then taking the partial derivative along the z direction is equivalent to taking the normal derivative, and the final boundary condition we obtain is

$$U_\infty^2 \frac{\partial^2 \phi}{\partial x^2} + g \frac{\partial \phi}{\partial n} = 0, \tag{16}$$

which is what we impose on the undisturbed free surface. The free surface elevation can be computed by postprocessing the flow potential through equation (14):

$$\eta = -\frac{U_\infty}{g} \frac{\partial \phi}{\partial x}. \tag{17}$$

2.3 Problem setup

We complete the problem by selecting the boundary conditions to be prescribed on the remaining boundary regions. On the body boundary Γ_{body} we impose a —non-homogeneous Neumann— non penetration condition. Homogeneous Neumann conditions are instead imposed on the lateral truncation surfaces Γ_{tank} of the numerical tank. The same condition is imposed on the outflow boundary Γ_{out}, while a homogeneous Dirichlet boundary condition is imposed on the inflow boundary Γ_{in}. The latter condition is selected in order to avoid a pure Neumann boundary problem, the solution of which would be defined only up to a constant. The complete boundary value problem reads:

$$\begin{aligned}
-\Delta\phi &= 0 && \text{in } \Omega && \text{(18a)}\\
\frac{\partial \phi}{\partial n} &= -\mathbf{v}_\infty \cdot \mathbf{n} && \text{on } \Gamma_{body} && \text{(18b)}\\
\frac{\partial \phi}{\partial n} &= -\frac{U_\infty^2}{g} \frac{\partial^2 \phi}{\partial x^2} && \text{on } \Gamma_{fs} && \text{(18c)}\\
\frac{\partial \phi}{\partial n} &= 0 && \text{on } \Gamma_{out} \cup \Gamma_{tank} && \text{(18d)}\\
\phi &= 0 && \text{on } \Gamma_{in}. && \text{(18e)}
\end{aligned}$$

It must be pointed out that the homogeneous Neumann conditions prescribed on the truncation surfaces might result in an undesired reflection of water waves back in the flow domain (see [24]). To limit this problem, in this work we employed a computational domain of considerable dimensions. The lateral truncation

boundaries Γ_{tank} are located in fact at a distance $15 \times L$ from the origin, while the Γ_{in} and Γ_{out} surfaces are at distances $15 \times L$ and $15 \times L$ from the origin respectively, where L is the length of the body.

2.4 Boundary integral formulation

Following [6], we exploit the second Green identity and reformulate Laplace equation (18a) as

$$\int_\Omega (-\Delta\phi) G \, \mathrm{d}x = \int_\Omega (-\Delta G)\phi \, \mathrm{d}x + \int_\Gamma \frac{\partial \phi}{\partial \mathbf{n}} G \, \mathrm{d}s - \int_\Gamma \phi \frac{\partial G}{\partial \mathbf{n}} \, \mathrm{d}s = 0, \tag{19}$$

where $\mathbf{n}$ is the outward normal to Γ while G is the so called free-space Green function, or fundamental solution of the Laplace equation, also known as the Rankine source, namely:

$$G(\mathbf{x} - \mathbf{y}) = \frac{1}{4\pi} \frac{1}{|\mathbf{x} - \mathbf{y}|}. \tag{20}$$

The Rankine source satisfies, in a distributional sense, the equation

$$-\Delta G(\mathbf{x} - \mathbf{y}) = \delta(\mathbf{x} - \mathbf{y}). \tag{21}$$

Exploiting this property, equation (19) can be rewritten as

$$\phi(\mathbf{x}) = \int_\Gamma G(\mathbf{x} - \mathbf{y}) \frac{\partial \phi}{\partial n}(\mathbf{x}) \, \mathrm{d}s_y - \int_\Gamma \phi(\mathbf{x}) \frac{\partial G}{\partial n}(\mathbf{x} - \mathbf{y}) \, \mathrm{d}s_y \qquad \forall \mathbf{x} \in \Omega. \tag{22}$$

We point out that equation (22) allows for the computation of the potential ϕ in any point $\mathbf{x}$ in the domain Ω if $\phi(\mathbf{x})$ and its normal derivative $\frac{\partial \phi}{\partial n}(\mathbf{x})$ are known on the boundary Γ. If we move the point $\mathbf{x}$ towards the boundary Γ, the kernels $G(\mathbf{x} - \mathbf{y})$ and $\frac{\partial G}{\partial n}(\mathbf{x} - \mathbf{y})$ become weakly singular (but integrable) and singular respectively. Considering the Cauchy Principal Value (CPV) of the singular integral, we can write the boundary integral form of the original problem as

$$\begin{aligned}
\alpha(\mathbf{x})\phi(\mathbf{x}) =& \int_\Gamma G(\mathbf{x} - \mathbf{y}) \tfrac{\partial \phi}{\partial n}(\mathbf{x}) \, \mathrm{d}s_y - \int_\Gamma^{PV} \phi(\mathbf{x}) \tfrac{\partial G}{\partial n}(\mathbf{x} - \mathbf{y}) \, \mathrm{d}s_y && \text{on } \Gamma && \text{(23a)} \\
\frac{\partial \phi}{\partial n} =& -\mathbf{v}_\infty \cdot \mathbf{n} && \text{on } \Gamma_{body} && \text{(23b)} \\
\frac{\partial \phi}{\partial n} =& -\frac{U_\infty^2}{g} \frac{\partial^2 \phi}{\partial x^2} && \text{on } \Gamma_{fs} && \text{(23c)} \\
\frac{\partial \phi}{\partial n} =& \, 0 && \text{on } \Gamma_{out} \cup \Gamma_{tank} && \text{(23d)} \\
\phi =& \, 0 && \text{on } \Gamma_{in}, && \text{(23e)}
\end{aligned}$$

where the coefficient $\alpha(\mathbf{x})$ appearing in the left hand side of equation (23) is obtained from the CPV evaluation of the singular integral on the right hand side, and represents the fraction of solid angle with which the domain Ω is seen from the boundary point $\mathbf{x}$. Equation (23a) is also known as Boundary Integral Equation (BIE).

3 Numerical approximation by boundary element method

Boundary integral formulations only involve functions defined on the boundary Γ of the computational domain Ω. In order to solve numerically such a problem, it suffices to provide an approximation of the surfaces making Γ and to define finite dimensional functional spaces *on the boundary only*.

We use standard Lagrangian finite element spaces on Γ to define both the geometry and the basis functions for ϕ and $\frac{\partial \phi}{\partial n}$. These basis functions are of interpolatory type, in the sense that they are defined through a set of *support points* $\mathbf{x}_j$ where they may only be zero or one, and each basis function has value one in a unique support point.

The two unknowns of our problem, namely ϕ and $\frac{\partial \phi}{\partial n}$, have different mathematical characteristics. While the potential ϕ is a continuos function on Γ, $\frac{\partial \phi}{\partial n}$ depends on the normal vector $\mathbf{n}$ which is discontinuos across the edges of Γ. In order to provide an accurate numerical solution, it is crucial to choose a different numerical representation for ϕ and $\frac{\partial \phi}{\partial n}$. The approximation of the boundary Γ of the domain should be continuos, and we represent it through the same basis functions that we use for the potential ϕ. Our approximation is isoparametric in the first unknown ϕ, and it allows for discontinuities across edges for $\frac{\partial \phi}{\partial n}$. We refer to this type of approximation as Mixed Isoparametric BEM. The unknowns of the problem are the values of ϕ and $\frac{\partial \phi}{\partial n}$ on the respective set of support points.

The approximation of the geometry of Γ and the choice of the proper spaces are exploited at the discrete level by an approximation procedure divided in five main steps:

Computational mesh creation: introduce a computational mesh which is a regular decomposition Γ_h of the boundary Γ made of quadrilateral cells (here *regular* means that any two cells K, K' only intersects on common faces, edges or vertices);

Definition of the discrete spaces: introduce two (*a priori* independent) finite dimensional spaces V_h and Q_h, [1] defined on Γ_h, such that

$$V_h := \left\{\phi_h \in C^0(\Gamma_h) : \phi_{h|K} \in \mathbb{Q}^r(K),\ K \in \Gamma_h\right\} \equiv \text{span}\{\psi_i\}_{i=1}^{N_V} \tag{25a}$$

$$Q_h := \left\{\gamma_h \in L^2(\Gamma_h) : \gamma_{h|K} \in \mathbb{Q}^s(K),\ K \in \Gamma_h\right\} \equiv \text{span}\{\omega_i\}_{i=1}^{N_Q}, \tag{25b}$$

where on each cell K, located on the boundary, $\phi_{h|K}, \gamma_{h|K}$ are polynomial functions of degree r and s respectively, in each coordinate direction. The corresponding Lagrangian basis functions of the spaces V_h and Q_h are denoted ψ_i and ω_i respectively;

Collocation of the Boundary Integral Equations: replace the continuous functions ϕ and $\frac{\partial\phi}{\partial n}$ by their numerical approximations ϕ_h and γ_h, which represent the discretised potential and potential normal derivative respectively in V_h and Q_h, and collocate the BIE on the correct support ponts on the boundary Γ_h;

Imposition of the boundary conditions: compute the boundary condition for ϕ_h and γ_h, by L^2 projection for the potential normal and second derivatives;

Solution of the linear system: the procedure above leads to a (dense) linear system which is solved either directly or iteratively.

3.1 Geometry and variable representations

When the Lagrangian basis functions for V_h and Q_h are given by ψ_i and ω_i respectively, a finite dimensional approximation of the unknowns ϕ and $\frac{\partial\phi}{\partial n}$ reads

$$\phi\Big|_\Gamma(\mathbf{x}) \sim \phi_h(\mathbf{x}_h) = \sum_{i=1}^{N_V} \psi_i(\mathbf{x}_h)\phi_i \qquad \mathbf{x} \in \Gamma, \quad \mathbf{x}_h \in \Gamma_h \tag{26}$$

$$\frac{\partial\phi}{\partial n}\Big|_\Gamma(\mathbf{x}) \sim \gamma_h(\mathbf{x}_h) = \sum_{i=1}^{N_Q} \omega_i(\mathbf{x}_h)\gamma_i \qquad \mathbf{x} \in \Gamma, \quad \mathbf{x}_h \in \Gamma_h. \tag{27}$$

[1] For the integrals in equation (23a) to be bounded, ϕ and $\frac{\partial\phi}{\partial n}$ must lie in the spaces V and Q, defined as

$$V := \left\{\phi \in H^{\frac{1}{2}}(\Gamma)\right\} \tag{24a}$$

$$Q := \left\{\gamma \in H^{-\frac{1}{2}}(\Gamma)\right\}, \tag{24b}$$

where $\Gamma = \partial\Omega$. We recall that $H^{\frac{1}{2}}(\Gamma)$ can be defined as the space of traces on Γ of functions in $H^1(\Omega)$, while $H^{-\frac{1}{2}}(\Gamma)$ is its dual space. The spaces V_h and Q_h are constructed as conforming finite dimensional subspaces of V and Q respectively.

Here $\{\psi_i\}$ and $\{\omega_i\}$ have the cardinality N_V and N_Q of the corresponding finite element spaces, and are defined *only* on the approximated boundary Γ_h. In particular, they can be conveniently expressed in terms of a *local coordinate system* (u, v) on each element K, by introducing for both V_h and Q_h, the set of *local basis functions*, a *mapping* from a reference element to the real geometric element K and a *local to global* numbering map k_i (see Figure 3).

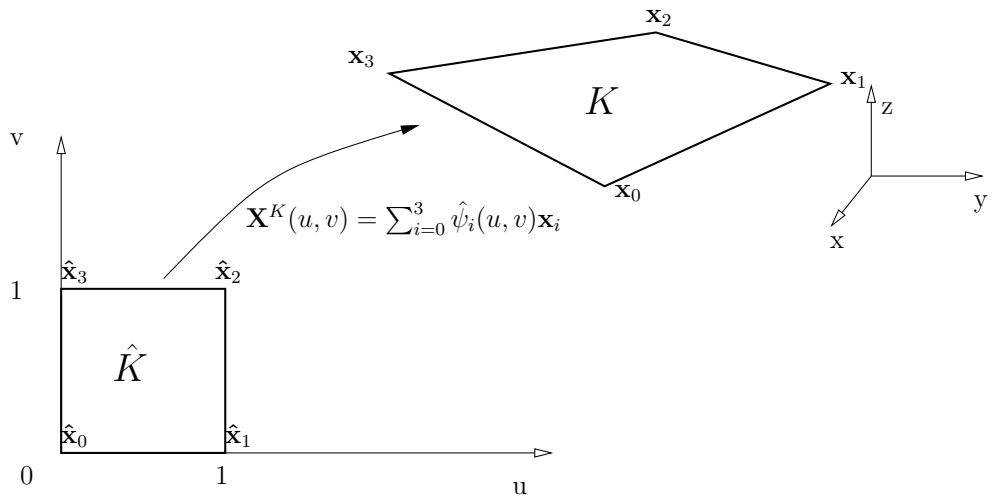

Figure 3: Transformation from reference to real cell. In this example we have considered a linear continuous approximation for the geometry, with support points on the vertices of the quadrilateral. The BEM is isoparametric because the geometry is described by the same finite element approximation of the potential ϕ.

In particular, we can define the approximation of the global basis functions restricted on $K \subset \Gamma_h$ as functions of the reference variables u and v on K:

$$\mathbf{X}^K(u,v) = \sum_{m=0}^{3} \hat{\psi}_m(u,v)\mathbf{x}_{i_m} \qquad i_m \in \{1,\ldots,N_V\} \tag{28a}$$

$$\hat{\psi}_m(u,v) = \psi_{i_m^K}(\mathbf{X}^K(u,v)), \qquad i_m^K \in \{1,\ldots,N_V\}, \quad m \in \{0,1,2,3\} \tag{28b}$$

$$\hat{\omega}_m(u,v) = \omega_{a_m^K}(\mathbf{X}^K(u,v)), \qquad a_m^K \in \{1,\ldots,N_Q\}, \quad m \in \{0,1,2,3\}. \tag{28c}$$

3.2 BEM: collocation technique

A discrete form of the BIE (23a) is obtained by replacing the continuous solutions ϕ and $\frac{\partial \phi}{\partial n}$ by their finite dimensional approximations ϕ_h and γ_h, and imposing the original boundary integral equation at a sufficient number of *collocation points*. Such collocation points are placed in correspondance with the N_V support points

of the V_h space and, with the N_Q support points of the Q_h space. Thus we obtain a system of $N_V + N_Q$ algebraic equations which reads respectively,

$$\begin{bmatrix} \mathbf{H^V} & \mathbf{D^V} \\ \mathbf{H^Q} & \mathbf{D^Q} \end{bmatrix} \begin{Bmatrix} \boldsymbol{\phi} \\ \boldsymbol{\gamma} \end{Bmatrix} = \begin{Bmatrix} 0 \\ 0 \end{Bmatrix}, \tag{29}$$

where

$$\boldsymbol{\phi} = \{\phi_1, \ldots, \phi_{N_V}\}, \boldsymbol{\gamma} = \left\{\gamma_1, \ldots, \gamma_{N_Q}\right\}.$$

are the vectors containing the unknown values of the the approximated functions ϕ_i and γ_i at each collocation point. In the block system (29), the matrix rows in the top blocks are the ones obtained collocating the BIE on the N_V support points corresponding to the potential degrees of freedom, while the matrix rows in the bottom blocks are obtained using the N_Q support points of the normal derivative as collocation points.

All integrations are performed on a planar reference domain, i.e. we assume that each element K_i of Γ_h as a transformation of the reference boundary element $\hat{K} := [0,1]^2$, as depicted in Figure 3.The integrations are performed after a change of variables from the real element K_i to the reference element $\hat{K}$.
Given a collocation point $\mathbf{P}_i$ of the potential ϕ, the block matrix entries read

$$H^V_{ij} = \alpha(\mathbf{P}_i) + \sum_{K=1}^{M} \int_0^1 \int_0^1 \frac{\partial G}{\partial n}(\mathbf{P}_i - \mathbf{X}^K(u,v))\hat{\psi}_j(u,v)J^K(u,v)\,\mathrm{d}u\,\mathrm{d}v, \tag{30a}$$

$$D^V_{ib} = \sum_{K=1}^{M} \int_0^1 \int_0^1 G(\mathbf{P}_i - \mathbf{X}^K(u,v))\hat{\omega}_b(u,v)J^K(u,v)\,\mathrm{d}u\,\mathrm{d}v, \tag{30b}$$

while if $\mathbf{Q}_a$ is a γ collocation point, we have

$$H^Q_{aj} = \alpha(\mathbf{Q}_a) + \sum_{K=1}^{M} \int_0^1 \int_0^1 \frac{\partial G}{\partial n}(\mathbf{Q}_a - \mathbf{X}^K(u,v))\hat{\psi}_j(u,v)J^K(u,v)\,\mathrm{d}u\,\mathrm{d}v, \tag{30c}$$

$$D^Q_{ab} = \sum_{K=1}^{M} \int_0^1 \int_0^1 G(\mathbf{Q}_a - \mathbf{X}^K(u,v))\hat{\omega}_b(u,v)J^K(u,v)\,\mathrm{d}u\,\mathrm{d}v, \tag{30d}$$

where M is the total number of elements K of the triangulation Γ_h, J^K is the Jacobian of the mapping $\mathbf{X}^K$ in the K-th element and the indices i, j run from one to N_V, while the indices a, b run from one to N_Q.

Due to the possible presence of singular kernels, the integrals in equations (30) require special treatment. In this work, standard Gauss quadrature rules are used for panels not containing singularities while for panels containing singular kernel values, we use Telles' quadrature rule [26].

Block system (29) is ill posed and cannot be used to obtain a numerical solution of problem (23), since i) it does not contain any information about boundary conditions and ii), it might have identical rows if some support points of ϕ and γ coincide. Notice that usually, on any given region of Γ, either ϕ is known and $\gamma = \frac{\partial \phi}{\partial n}$ is unknown, or the opposite. The free surface condition (equation 23c) is an exception to this rule, and can be seen as special case of Robin boundary condition. On the free surface both ϕ and $\frac{\partial \phi}{\partial n}$ are unknown, but we impose a linear relationship between $\frac{\partial \phi}{\partial n}$ and a differential operator on ϕ.

While at the continuous level this relationship is easily derived from the perturbation analysis of section 2.2, at the discrete level the application of this theory is non trivial since the spaces V_h and Q_h are in general different, and some care should be taken if one wants to obtain a consistent approximation, with good numerical properties.

To fix the ideas, consider the boundary Γ as the union of three disjoint sets, consisting of the Neumann boundary portion $\Gamma_N = \Gamma_{body} \cup \Gamma_{out} \cup \Gamma_{tank}$, the Dirichlet boundary portion $\Gamma_D = \Gamma_{in}$ and the Robin boundary portion $\Gamma_R = \Gamma_{fs}$. Both ϕ and γ can then be separated into their Neumann, Dirichlet and Robin parts respectively, according to the location of the support points.

Assuming that $\boldsymbol{\phi}_D$ is known on the Dirichlet portion Γ_D, $\boldsymbol{\gamma}_N$ is known on the Neumann portion Γ_N and that we have a pair of linear operators $\mathbf{D}$ and $\mathbf{M}$ such that $\mathbf{D}\boldsymbol{\phi}_R + \mathbf{M}\boldsymbol{\gamma}_R = \bar{\mathbf{c}}_R$, then system (29) can be solved explicitly by imposing the boundary conditions instead of the boundary integral equations in the appropriate lines of system (29):

$$\begin{bmatrix} \mathbf{H^V}_{NN} & \mathbf{H^V}_{ND} & \mathbf{H^V}_{NR} & \mathbf{D^V}_{NN} & \mathbf{D^V}_{ND} & \mathbf{D^V}_{NR} \\ 0 & \mathbf{I}_{DD} & 0 & 0 & 0 & 0 \\ \mathbf{H^V}_{RN} & \mathbf{H^V}_{RD} & \mathbf{H^V}_{RR} & \mathbf{D^V}_{RN} & \mathbf{D^V}_{RD} & \mathbf{D^V}_{RR} \\ 0 & 0 & 0 & \mathbf{I}_{NN} & 0 & 0 \\ \mathbf{H^Q}_{DN} & \mathbf{H^Q}_{DD} & \mathbf{H^Q}_{DR} & \mathbf{D^Q}_{DN} & \mathbf{D^Q}_{DN} & \mathbf{D^Q}_{DR} \\ 0 & 0 & \mathbf{D} & 0 & 0 & \mathbf{M} \end{bmatrix} \begin{Bmatrix} \boldsymbol{\phi}_N \\ \boldsymbol{\phi}_D \\ \boldsymbol{\phi}_R \\ \boldsymbol{\gamma}_N \\ \boldsymbol{\gamma}_D \\ \boldsymbol{\gamma}_R \end{Bmatrix} = \begin{Bmatrix} 0 \\ \bar{\boldsymbol{\phi}}_D \\ 0 \\ \bar{\boldsymbol{\gamma}}_N \\ 0 \\ \bar{\mathbf{c}}_R \end{Bmatrix}. \quad (31)$$

Notice that the boundary integral equations in system (31) are evaluated only once in each region, and that, in principle, one could solve Robin's boundary condition by either imposing $\boldsymbol{\phi}_R$ and extracting $\boldsymbol{\gamma}_R$ from the linear combination, or by imposing $\boldsymbol{\gamma}_R$ and extracting $\boldsymbol{\phi}_R$. This alternative approach would result in line 6 of system (31) to be swapped with line 3, evaluating the boundary integral equations on support points of Q_h instead of V_h, i.e., replacing $\mathbf{H^V}$ and $\mathbf{D^V}$ by $\mathbf{H^Q}$ and $\mathbf{D^Q}$ respectively.

3.3 Imposition of boundary conditions

Dirichlet boundary conditions can be imposed directly by substituting the corresponding line of the matrix system (29) with a new line only composed by a value of 1 on the matrix diagonal, and by the prescribed value of ϕ on the right hand side vector, just as in system (31).

The imposition of the correct Neumann boundary condition is not so straightforward. If the field $\frac{\partial \phi}{\partial n}$ is directly available on the collocation points, the procedure is identical to the Dirichlet boundary condition. This is for example the case for condition (23d). In several practical cases, however, the value of $\frac{\partial \phi}{\partial n}$ may not be available on all collocation points. An example of this situation is given by the non penetration condition (23b). If the surface is approximated with the panel patches illustrated in Figure 3, the surface boundary normal is not single valued in correspondence of the collocation points which are located on the edges or vertices of the panels.

In these cases, the prescribed potential normal derivative value $-\mathbf{v}_\infty \cdot \mathbf{n}$ is in principle not defined, and we need to make a choice on what it means to consider $\frac{\partial \phi}{\partial n}$ on that particular collocation point. This situation is not new to this method, and it exists since the introduction of the Finite Element Method. However, when using the Finite Element Method, *weak forms* of the equations are always written (and not *point evaluations*), which ditch the issue by evaluating normals and normal derivatives *only on the interior of the quadrilaterals*. Similarly, piecewise constant approximations of ϕ and $\frac{\partial \phi}{\partial n}$ in boundary element methods, which are often referred to as *panel methods*, allow the collocation of the support points on the *center* of the cells, avoiding all places where $\frac{\partial \phi}{\partial n}$ might not be single valued, like edges and vertices.

Higher order collocation BEMs must confront with these issues, one way or another, since it is common for higher order finite dimensional spaces to have support points defined also on edges and vertices. In this work we exploit a common technique used in the finite element community: the L_2 projection. Multiplying equation (23b) by a test function $u \in Q$, and integrating over Γ results in

$$\int_\Gamma \gamma u \, \mathrm{d}\Gamma = \int_\Gamma -\mathbf{V}_\infty \cdot \mathbf{n} u \, \mathrm{d}\Gamma \quad \forall u \in Q \tag{32}$$

which is a weak form of the original boundary condition. This problem is discretised by means of the finite dimensional approximation Q_h of the solution space Q. In this framework, $\gamma = \frac{\partial \phi}{\partial n}$ is approximated as in equation (27). If equation (32) must now hold for any function $u_h \in Q_h$, it will be sufficient to test such equation for each of the N_Q basis functions of Q_h. This results in the linear system

$$\mathbf{M^Q}\, \boldsymbol{\gamma} = \mathbf{b}, \tag{33}$$

where the generic element of $\mathbf{M^Q}$ is given by

$$M^Q_{ab} = \int_\Gamma \omega_b(\mathbf{x})\omega_a(\mathbf{x})\,\mathrm{d}\Gamma, \quad a, b = \{1, \ldots, N_Q\} \tag{34}$$

and each component of the right hand side vector $\mathbf{b}$ is assembled as follows

$$\mathbf{b}_a = -\int_\Gamma (\mathbf{V}_\infty \cdot \mathbf{n}(\mathbf{x}))\,\omega_a(\mathbf{x})\,\mathrm{d}\Gamma, \quad a = \{1, \ldots, N_Q\}. \tag{35}$$

The mass matrix $\mathbf{M^Q}$ is sparse, since every basis function ω_a has compact support. In principle, this system could be solved separately to obtain the values of $\gamma = \frac{\partial\phi}{\partial n}$ to be applied in BEM system (31). In practice, though, it is more convenient to "mix" system (31) and system (33). In this framework, the rows of the BEM system corresponding to Neumann nodes are substituted with the matching rows in system (33). So, in a way we are enriching the boundary element method with techniques coming from a finite element approach, which are applied *only on the surface* Γ, to preserve the dimensional reduction typical of BEM.

The BEM approach allows for the discretisation of the domain boundary only, while treating boundary condition in weak form with a FEM approach helps dealing with non-continuous boundary data. This is particularly important when considering the linearised free surface boundary condition (23c).

3.4 Treatment of the linearised free surface condition

The discretisation of the linearised free surface boundary condition presents the same problems discussed for Neumann conditions in section 3.3, since the partial derivative on the right hand side of equation (23c) could be, in principle, not single valued on the collocation points, when these are located on the edges or on the vertices of the panels. We reformulate this condition in weak form, and we discretise it by means of a FEM approach similar to the one described in the previous section.

The presence of second order derivatives in the right hand side of the free surface boundary condition requires a careful treatment. Consider, for example, the case of linear finite dimensional spaces V and Q: in this case, the second order derivatives on each panel would be identically zero.

A solution which is consistent with the approximation of the Neumann boundary conditions, consists in introducing an additional variable β (which we assume to be in the same space V of the potential ϕ), representing $\frac{\partial\phi}{\partial x}$, and to recover both the variable itself and its derivative using a weak formulation. Namely:

$$\int_\Gamma \beta v\,\mathrm{d}\Gamma = \int_\Gamma \frac{\partial}{\partial x}\phi v\,\mathrm{d}\Gamma \qquad \forall v \in V \tag{36}$$

$$\int_\Gamma \gamma u \, \mathrm{d}\Gamma = -\frac{U_\infty^2}{g} \int_\Gamma \frac{\partial}{\partial x} \beta u \, \mathrm{d}\Gamma \qquad \forall u \in Q. \tag{37}$$

The function β appearing in equations (36) and (37) is approximated as

$$\beta_h(\mathbf{x}) = \sum_{i=1}^{N_V} \psi_i(\mathbf{x}) \beta_i. \tag{38}$$

Using the finite dimensional spaces, equation (36) can be recast in the following form

$$[\mathbf{M^V}]\boldsymbol{\beta} - [\mathbf{B^V}]\boldsymbol{\phi} = 0, \tag{39}$$

where

$$M_{ij}^V = \int_\Gamma \psi_j(\mathbf{x}) \psi_i(\mathbf{x}) \, \mathrm{d}\Gamma, \quad i,j = \{1, \ldots, N_V\} \tag{40a}$$

$$B_{ij}^V = \int_\Gamma \frac{\partial \psi_j(\mathbf{x})}{\partial x} \psi_i(\mathbf{x}) \, \mathrm{d}\Gamma, \quad i,j = \{1, \ldots, N_V\}. \tag{40b}$$

In the present work, we used the same approximation space for β and for the potential ϕ, even though the spaces could in principle be different. The additional variable β adds to the global algebraic system a set of N_V sparse rows obtained by the discretisation of equation (36). This system represents an additional block in the complete BEM system. The three unknown vectors of the system are now $\boldsymbol{\phi}, \boldsymbol{\gamma}, \boldsymbol{\beta}$. Along the same lines, the discretised form of equation (37) assumes the form

$$[\mathbf{M^Q}]\boldsymbol{\gamma} + \frac{U_\infty^2}{g}[\mathbf{B^{QV}}]\boldsymbol{\beta} = 0, \tag{41}$$

where $\mathbf{M^Q}$ is given by equation (34), while the elements of $\mathbf{B^{QV}}$ are given by

$$B_{aj}^{QV} = \int_\Gamma \frac{\partial \psi_j(\mathbf{x})}{\partial x} \omega_a(\mathbf{x}) \, \mathrm{d}\Gamma, \quad a = \{1, \ldots, N_Q\}, \quad j = \{1, \ldots, N_V\}. \tag{42}$$

The lines of this system are substituted to the lines of the BEM subsystem corresponding to the collocation points of the normal derivative approximation that are located on the free surface. Another derivation in weak form is applied to $\boldsymbol{\beta}$, which is then projected using an L^2 projection in the space Q_h to obtain a weak form of the second derivative ($\partial^2\phi/\partial x^2$) appearing in the right hand side of the linearised free surface boundary condition (37), in the same space of the normal derivative of the potential (Q_h). The additional variable $\boldsymbol{\beta}$ can be easily eliminated by inverting the mass matrix $\mathbf{M^V}$ and setting

$$\mathbf{C^Q} := \frac{U_\infty^2}{g}\mathbf{B^{QV}}(\mathbf{M^V})^{-1}\mathbf{B^V}. \tag{43}$$

$[\mathbf{D}]\{\boldsymbol{\phi}\}$ is a *weak* approximation of $\left(\frac{U_\infty^2}{g}\frac{\partial^2\phi}{\partial x^2}\right)$, i.e., it is its L^2 projection on the space Q_h. The final system of equations can be written in compact form as

$$\begin{bmatrix} \mathbf{H^V}_{NN} & \mathbf{H^V}_{ND} & \mathbf{H^V}_{NR} & \mathbf{D^V}_{NN} & \mathbf{D^V}_{ND} & \mathbf{D^V}_{NR} \\ 0 & \mathbf{I}_{DD} & 0 & 0 & 0 & 0 \\ \mathbf{H^V}_{RN} & \mathbf{H^V}_{RD} & \mathbf{H^V}_{RR} & \mathbf{D^V}_{RN} & \mathbf{D^V}_{RD} & \mathbf{D^V}_{RR} \\ 0 & 0 & 0 & \mathbf{M^Q}_{NN} & 0 & 0 \\ \mathbf{H^Q}_{DN} & \mathbf{H^Q}_{DD} & \mathbf{H^Q}_{DR} & \mathbf{D^Q}_{DN} & \mathbf{D^Q}_{DN} & \mathbf{D^Q}_{DR} \\ 0 & 0 & \mathbf{C^Q}_{RR} & 0 & 0 & \mathbf{M^Q}_{RR} \end{bmatrix} \begin{Bmatrix} \boldsymbol{\phi}_N \\ \boldsymbol{\phi}_D \\ \boldsymbol{\phi}_R \\ \boldsymbol{\gamma}_N \\ \boldsymbol{\gamma}_D \\ \boldsymbol{\gamma}_R \end{Bmatrix} = \begin{Bmatrix} 0 \\ \mathbf{0}_D \\ 0 \\ \mathbf{b}_N \\ 0 \\ \mathbf{0}_R \end{Bmatrix}, \quad (44)$$

where only the $\mathbf{H}$ and $\mathbf{D}$ matrices are full, while all other matrices appearing in system (44) are sparse.

3.5 Streamwise upwind Petrov Galerkin stabilisation

The numerical strategy presented in the previous sections generates an accurate approximation of the second order derivative appearing in the linearised free surface boundary condition. Yet, this is not sufficient to obtain a physically meaningful approximation of problem (23e), due to two issues of different nature: i) the boundary condition (23c) is symmetrical in the x direction and ii) the problem is transport dominated.

If a physical wave propagating downstream with respect to the stream velocity $\mathbf{v}_\infty$ fulfils the linearised condition, also an unphysical wave propagating upstream will satisfy such condition. Several different methodologies have been developed over the years, to selectively suppress the nonphysical solution without affecting the physical waves. In this work, we impose a homogeneous Dirichlet condition on the inflow surface of the domain, and a homogeneous Neumann condition on the outflow, as suggested in [24]. This setup satisfies a radiation condition and breaks the symmetry of the solutions in the x direction, privileging only the physical solution.

While in principle this should be sufficient, the problem at hand is transport dominated, and instabilities occur whenever a non-negligible fluid velocity is considered. In [10], Dawson stabilised the transport problem, while at the same time suppressing the unphysical upstream waves, using upwind finite differences for the approximation of the second order derivative in (23c). Although this strategy proved to be successfull, it presents two main drawbacks: i) it introduces a considerable amount of numerical dissipation and, more importantly, ii) it forces the use of structured meshes which do not allow for local refinement strategies.

The Streamline Upwind Petrov Galerkin (SUPG) method makes it possible to maintain the accuracy of the L^2 projection approach while evaluating the second

order derivative in the linearised free surface boundary condition. This is a powerful stabilisation technique which has been applied in a variety of frameworks, however its application to meshless methods [28] and boundary elements [17, 18] is very recent. A FEM-SUPG has already been coupled to a BEM problem in [13], in the framework of magnetohydrodynamic flows through a circular pipe. In that scenario a BEM tecnique is applied to recover the magnetic and velocity field outside the pipe while the FEM-SUPG framework is used to compute the fields inside the pipe. In the present work we used the FEM-SUPG technique to properly project the boundary conditions for the boundary element technique. In particular, the SUPG stabilisation is applied in a domain of codimension one. In the framework of SUPG stabilisation [2], we modify the generic shape function $H_i(\mathbf{x})$, used for finite elements approximation, in the following way

$$H_i^{SUPG}(\mathbf{x}) = H_j(\mathbf{x}) + \delta h \nabla_s H_i(\mathbf{x}) \cdot \frac{\mathbf{v}(\mathbf{x})}{||\mathbf{v}(\mathbf{x})||}. \tag{45}$$

Here the constant $0 \leq \delta \leq 1$ sets the local amount of upwind stabilisation on each cell. Since we work only on the boundary of our domain, the full gradient is replaced by the surface gradient ∇_s. The results in the present work are obtained considering $\delta = 1/\sqrt{2}$. As we worked with roughly square cells, and h represents the cell diameter, δh represents a good approximation of the streamwise cell dimension. Unfortunately, since the flow velocity is the main unknown of our simulations, the local velocity direction is not available at the time of the matrix assembling. However, the dominant component of the flow velocity is given by $\mathbf{v}_\infty$ and we can write the SUPG correction in terms of the asymptotic flow direction, namely

$$H_i^{SUPG}(\mathbf{x}) = H_i(\mathbf{x}) + \frac{1}{\sqrt{2}} h \nabla_s H_i(\mathbf{x}) \cdot \frac{\mathbf{v}_\infty}{||\mathbf{v}_\infty||}. \tag{46}$$

This SUPG strategy is used in equations (39) and (41) to modify the test functions ψ_i, ω_a into ψ_i^{SUPG} and ω_a^{SUPG}. In previous works, like [10] and [23], the second derivative in (37) is obtained directly through a finite difference scheme, requiring a structured grid and introducing consistency errors typical of finite differences. Since we make use of the variable $\boldsymbol{\beta}$ to compute such second derivative we have the possibility to enforce the SUPG stabilisation two times separately, *i.e.* once for each derivation along x. The most important advantage given by the use of the weak formulation combined with the SUPG stabilisation is that it allows the use of unstructured grids. In particular, it is possible to employ a free surface grid which is refined only near the body, or to adopt a local refinement strategy based on *a posteriori* error estimates. In addition, SUPG is a strongly consistent method and does not introduce numerical dissipation in the system.

3.6 Local Refinement

Unstructured grids call for a local refinement strategy, in order to concentrate the degrees of freedom where the solution has steeper gradients. We have chosen to use a modification of a simple and well known error estimator, originally proposed by Kelly, Gago, Zienkiewicz and Babuska, [1]. Such error estimator approximates the error on each cell by considering the L_2 norm of the jump of the surface gradient of the approximated solution across the cell boundaries. On each cell, the error indicator is computed as

$$\eta_K = \sqrt{\frac{h}{24} \int_{\partial K} [\mathbf{n}_{\partial K} \cdot \nabla_s u_h]^2 \, \mathrm{d}\sigma}. \tag{47}$$

The operator $[x]$ indicates the jump $x_{in} - x_{out}$, where x_{in} and x_{out} represent the values of the field x inside and outside the cell boundary respectively, $\mathbf{n}_{\partial K}$ is the outward unit normal to ∂K (laying on the same plane of K), and $\nabla_s u_h$ is the surface gradient of the field u_h.

The local refinement strategy has been set so that at every step thirty percent of cells with highest error estimator on the free surface are refined. We have chosen to keep the mesh fixed on the moving body, so that the local refinement is only active on the free surface. Once the refined mesh is available, a new simulation is carried out, and the procedure is repeated for the specified number of refinement cycles. When this iterative approach is used, the velocity field $\mathbf{v}^{old}$ obtained at the previous step is interpolated on the new grid and used to build the SUPG basis functions, namely

$$H_j(\mathbf{x})^{SUPG} = H_j(\mathbf{x}) + \alpha h \nabla_s H_j(\mathbf{x}) \cdot \frac{\mathbf{v}^{old}(\mathbf{x})}{||\mathbf{v}^{old}(\mathbf{x})||}. \tag{48}$$

This correction become important where the streamlines on the free surface are no more parallel to the x axis. In fact, if we consider a submerged body the streamlines on the free surface are practically aligned with the x axis, but in the case of surface piercing hull with rounded bow, this might not be the case. Figure 4 depicts different stages of the adaptive refinement cycles for the case of a fully submerged prolate spheroid. The pictures show that the cells tend to reach higher refinement levels on a pattern that follows the V-shaped Kelvin wake past the moving body. We remark that despite the additional cost of the refinement iterations, the local refinement strategy might be very useful. A global refinement strategy on structured mesh in fact, has an extremely high computational costs.

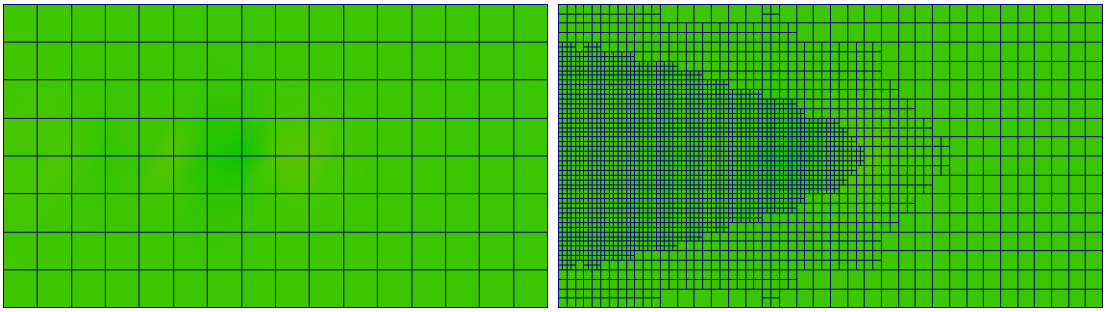

Figure 4: On the left, the free surface mesh at the initial level of refinement. On the right, the free surface mesh obtained after four refinement cycles

4 Numerical validation

To validate the behavior of our method in the treatment of free surface flows, two different problems are considered. In the first test case we have treated the motion of a fully submerged prolate spheroid at constant speed. In the second problem we have considered the stationary motion of a surface piercing body, the Wigley hull.

These flows are common benchmarks in the naval literature, so there are many available references to evaluate the accuracy of the method we developed.

4.1 Submerged prolate spheroid

The purpose of this section is to study the flow field past a fully submerged prolate spheroid advancing at constant speed in calm water. The domain we have considered is a box of fluid surrounding the spheroid. The longest axis of the spheroid is oriented along the x axis of the global frame of reference. The spheroid has been placed at a prescribed depth, intended as the distance between the main axis and the free surface. The free surface portion considered is represented by the upper face of the parallelepiped. The truncation faces of the domain, $\Gamma_{in} \bigcup \Gamma_{out} \bigcup \Gamma_{tank}$ in Fig. 5 are placed far enough from the spheroid, so as not to influence the solution near it. The considered prolate spheroid has an axis of length 5m along the x direction, of length 1 meter along y direction, axis of length 1 meter along z direction. So we compute $L_{sph} = 10$m.

The domain extends for $L_{\infty x} = 15 \times L_{sph}$ along the x axis, for $L_{\infty y} = 15 \times L_{sph}$ along the y and for $L_{\infty z} = 15 \times L_{sph}$ along the z axis. We chose a sufficient depth of the spheroid main axis in order to avoid the presence of strong nonlinear effects. A good depth is $d = 1.25 \times 4$m where 4_m is the diameter of the spheroid.
The overall height of the basin is enough to consider an infinite depth approximation. This will make possible a comparison between our data and the theory

introduced by Havelock in 1931, and reported in [14], which will be used here as a benchmark. Havelock derived an analytical expression for the the wave resistance of a spheroid submerged in water.

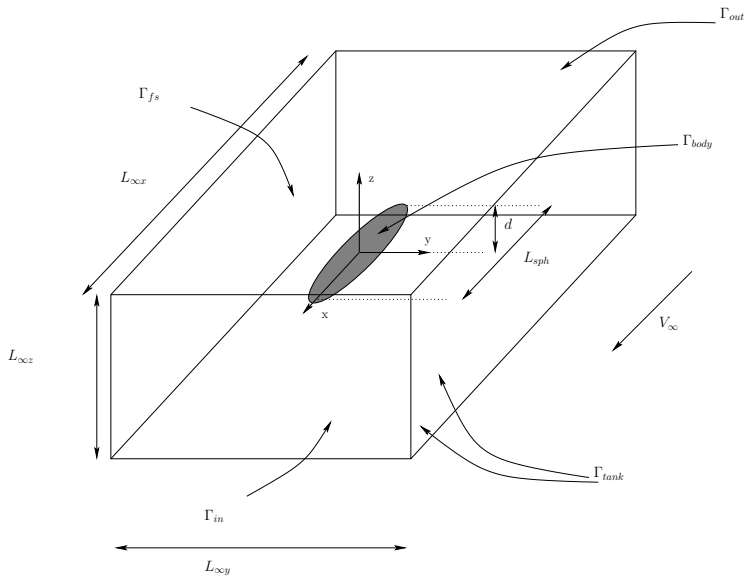

Figure 5: The spheroid is put under the free surface at a defined depth and it is possible to see also the outer tank set with $L_{\infty x}, L_{\infty y}, L_{\infty z}$. The flow enters from Γ_{in}, Γ_{tank} are the lateral surfaces and the bottom. The flow is considered at velocity V_∞ directed as the x axis.

The mesh on the spheroid is presented in Fig. 6. The grid is composed of 24 nodes along the longitudinal axis and of 4 nodes along the other two circular section. The free surface mesh is refined adaptively during the simulations, while the spheroid mesh is fixed.

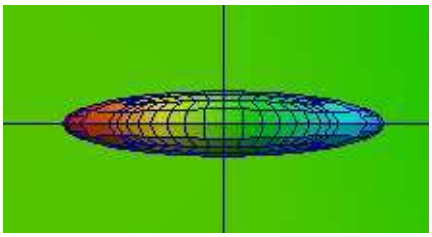

Figure 6: The fixed mesh on the prolate submerged spheroid.

4.1.1 Qualitative analysis of the wave pattern

We first want to highlight the importance of the SUPG method in the approximation of the second derivative in the linearised free surface boundary condition(see section 3.4). As example, we have chosen the flux with $U_\infty = 6\text{m/sec}$ and we show the isolines of the wave elevation, both when SUPG is used and not used in Fig. 7.

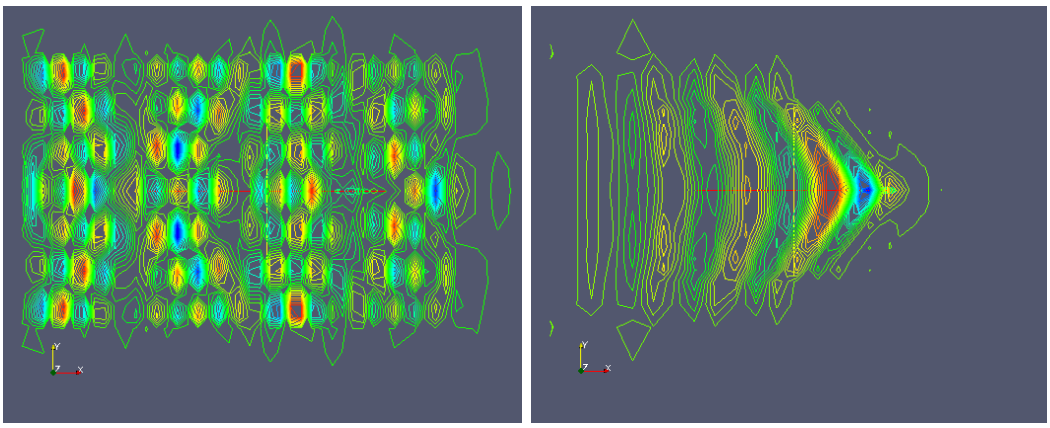

Figure 7: On the left, isolines representation of free surface elevation field for the chosen velocity $U_\infty = 2\text{m/sec}$ without the SUPG stabilisation. On the right, isolines representation of free surface elevation for $U_\infty = 2\text{m/sec}$ computed making use of the SUPG stabilisation. The colors on the contour lines represent the free surface elevation.

Looking at the plots we can appreciate that the SUPG stabilisation plays a key role in our model. As suggested in [10, 24] the addition of upwind terms in eq. (18c) suppresses the non physical upward propagating waves. In facts, we clearly see that without the SUPG there is a strong presence of waves which propagates upstream and any physical meaning of the solution is lost. Instead if we consider a SUPG stabilisation [2], the V-shaped Kelvin wake pattern is recovered. The SUPG stabilisation is a strongly consistent way of introducing upwinding in the linearised free surface condition. This is a first advantage because we introduce, using a strongly consistent method, less numerical dissipation in respect to a consistent method as an upwind finite difference stabilisation. Even more importantly the SUPG strategy allows us not to use structured grids. The purpose of the present section is to see whether the developed method leads to solutions that are consistent with what can be found in literature about the waves created by a submerged prolate spheroid.
In Fig. 8 we present contour plots of water elevation fields computed at different velocities, and at the same depth. We see that both elevation fields present clear V-shaped Kelvin wake patterns. Each wake is composed by a series of elevation

peaks located on lines inclined of about 20 with respect to the main stream axis. Between the two arms of the V-shaped pattern, we observe a series of transverse waves. As expected, increasing the velocity of the flow, we observe a growth of the wavelengths of both V-shaped and transverse waves. These two peculiarities may be more or less evident depending on the velocity of the spheroid, which in this section is commonly expressed in terms of Froude number, defined as

$$Fr = \frac{U_\infty}{\sqrt{gL_{spheroid}}}. \tag{49}$$

The wave angle has been indicated in Fig. 8 for $Fr = 0.5$ and for the $Fr = 0.7$, to confirm that the V-shape angle behaves consistently with the simple model described in [9],.

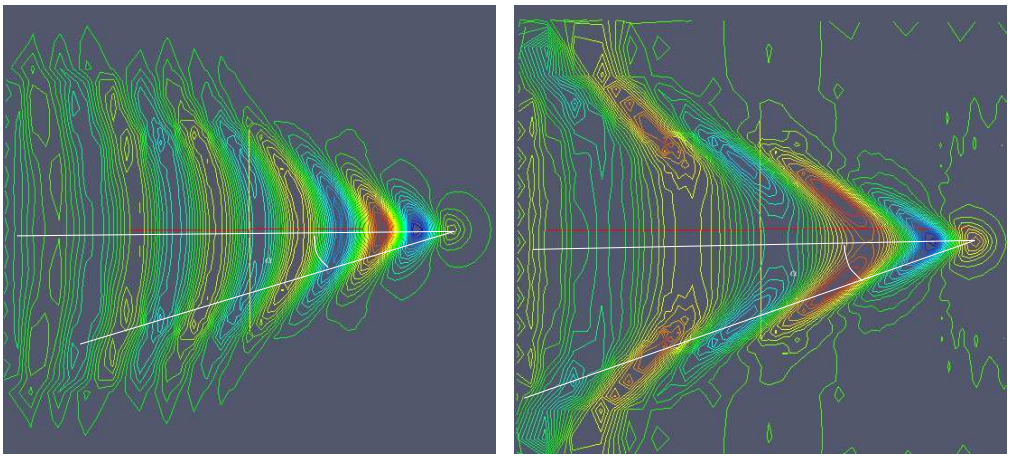

Figure 8: On the left, isolines representation of free surface elevation field for $Fr = 0.5$. On the right, isolines representation of free surface elevation for $Fr = 0.7$

At $Fr = 0.5$, an angle $\alpha = 16.11$ is observed, while at $Fr = 0.7$ the angle is of 18.02. This fact suggests that the developed method is able to reproduce one of the most important features of a Kelvin wake. We see also that for the lowest Froude number there is a clear presence of a transverse system which becomes less important at high Froude numbers, and this is well recovered. At $Fr = 0.7$ we can see that the peaks, called featherlets, are aligned on the V-shaped Kelvin wake.

4.1.2 Comparison with literature results

We extract the maximum absolute displacement of the free surface elevation from the reference value $z = \eta = 0$. These values are compared to the ones reported in [24]. In his work the authors employed a nonlinear steady potential

model. Even if the present method is based upon a linearised potential model, a comparison is still interesting. The curves of the wave elevation peak as a function of Fr number are presented in Fig. 9

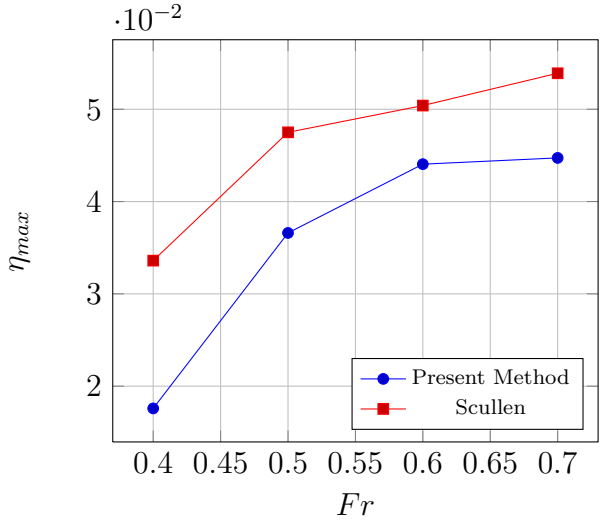

Figure 9: Maximum free surface elevation as a function of Froude number. The red line represents the results obtained using a non linear potential model, [24]. The blue line represent the results obtained with the present linearised potential method

The plot shows that the expected behavior is recovered by the model developed. Yet the our linear method underestimates the elevation obtained with the more general and accurate nonlinear method. This would be consistent with an underestimation of the wave drag on the spheroid. It is therefore interesting to analyze the drag induced by the wave generation. In [14] the authors managed to compute an analytical formula to predict the drag of a submerged spheroid. To obtain a closed form solution, the spheroid was approximated by a series of doublets with a uniform volume distribution and their axis parallel to the spheroid main axis which, in the present work, is the same direction as that of the external flow velocity. Calling the major semiaxis length a and the minor semiaxis length b:

$$e_c = \sqrt{1 - b^2/a^2} \tag{50}$$

$$A^{-1} = \frac{4e_c}{1 - e_c^2} - 2log\frac{1 + e_c}{1 - e_c} \tag{51}$$

$$D_w = 128\pi^2 g\rho a^3 e_c^3 A^2 e^{-p} \int_0^\infty e^{-pt^2} J_{3/2}(k_0 a e_c \sqrt{1 + t^2})\, \mathrm{d}t \tag{52}$$

Where $J_{3/2}$ is the Bessel function with base 3/2, $p = 2gf/u^2$, $k_0 = g/U_\infty$ and f is the depth of the spheroid major axis. Considering a spheroid with$f = 0.25$ it is possible to compute the drag coefficient predicted by this theory for the present test case. Introducing the spheroid length L and its diameter d, the drag coefficient is defined as.

$$C_w = \frac{D_w}{\pi/6\rho g L d^2} \tag{53}$$

Fig. 10 displays a comparison of wave drag coefficients between Havelock theory and the present method, for several values of Froude numbers (or of flow velocity). Recalling equation (8) we compute the pressure on the body as:

$$P = P_\infty + \frac{1}{2}\rho\left(U_\infty^2 - U^2\right) - \rho g z,$$

where z states for the height of the point in the considered framework. The drag coefficient can be obtained as the integral of the pressure coefficient as:

$$C_p = \frac{P - P_\infty}{1/2\rho U_\infty^2}$$
$$C_w = \frac{1/2\rho U_\infty^2}{\pi/6\rho g L d^2}\int_S C_p \,\mathrm{d}S$$

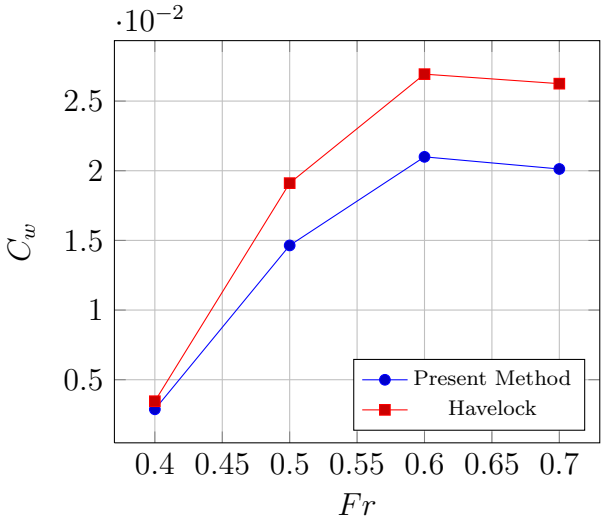

Figure 10: Wave drag coefficients of a fully submerged body as function of Froude number. The red line represents the analytical results as predicted by Havelock theory, [14]. The blue line represents the results of the present linearised potential model.

Again, the two curves show a similar behavior. The linearised model appears however to underestimate the drag, with respect to the analytical result. This error seems to be dependent on the Froude number, since it increases with the flow velocity. The same kind of error pattern has been observed also for different values of the depth f. This problem appears to be linked with what pointed out in Fig. 9. Since the our linearised model underestimates the height of the waves, it also underestimates the energy dissipated in the wave creation process, which leads to an underestimation of the drag force.

In the present work the wave coefficient only depends on the Froude number, as reported in [21] (page 31), in agreement with the so-called *Froude's hypothesis*. Such hypothesis states that the wave drag coefficient only depends on the Froude number, independently from the Reynolds number. *Froude's hypothesis* is confirmed by experimental data only when we are in presence of a thin boundary layer (theoretically of negligible thickness). This is verified especially for very big hulls, when the Reynolds number $Re = \rho U_\infty L_{boat}/\mu$ is higher than 10^5, where μ is the viscosity of the fluid. For our simulation, considered $L_{spheroid} = 10$ meters we have Re values between $3.5 \cdot 10^5$ and $5.7 \cdot 10^5$ so we respect the *Froude's hypothesis*.

4.1.3 Quadratic BEM

As a comparison with Higher Order BEM, we present the results obtained using the same spheroid presented in the previous section at Froude number $Fr = 0.7$ when the finite dimensional spaces are both quadratic.

Quadratic elements should be able to better approximate the derivative of the unknown ϕ appearing in the linearised free surface boundary condition. We have chosen to use quadratic continuous elements for ϕ, $\frac{\partial \phi}{\partial n}$ and $\partial\phi/\partial x$. We note that in order to obtain a meaningful results with quadratic elements we have used the well known Telles quadrature formula [26].

We report the final mesh after 4 local refinements.

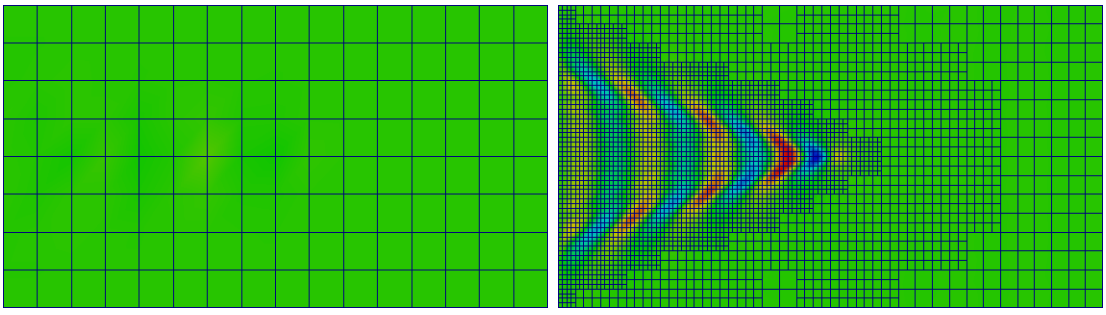

Figure 11: On the left the initial mesh. On the right the final mesh obtained in the submerged spheroid test case after 4 refinement cycles. Every 4 neighboring cells compose a single quadratic cell

We highlight that in Fig. 11 every four cells represent one quadratic cell. We can compare it with what we have previously obtained in the linear case, Fig. 4.

We report the comparison between what we have obtained in the linear case and this results with the quadratic, still continuous, BEM.

Table 1: Comparison between the quadrature formulas in the quadratic case at $Fr = 0.7$.

	Final C_w	Max wave height
LinearBEM	0.02099683	0.04405
QuadraticBEM	0.02120950	0.04436

The overall number of degrees of freedom is comparable between the two cases. So we have considered a less refined mesh for the higher order approximation. We see that, as we expected, the quadratic leads to a better approximation of the problem since the drag coefficient is increased and the wave pattern is better recovered.

4.2 Wigley hull

This section will describe how our model behaves in presence of a surface piercing body. The geometry considered for this test case, is that of Wigley hull. Given its simple analytic shape the Wigley hull is in fact a commonly used benchmark in hydrodynamics simulations, and several experimental data for such geometry are available in the literature.

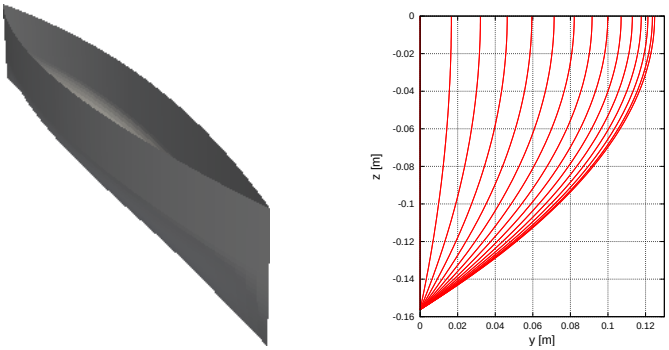

Figure 12: On the left, a three dimensional view of the Wigley hull used for the simulations. On the right vertical sections of the Wigley hull used for the simulations, generated by planes normal to the longitudinal axis of the hull.

The Wigley Hull is analytically described by the following equation

$$y(x,z) = \frac{B}{2}\left[1 - \left(\frac{2x}{L}\right)^2\right]\left[1 - \left(\frac{z}{T}\right)^2\right] (x,y) \in [-1,1]^2. \tag{54}$$

Where y is the span of the hull, x its length and z its depth; in the present calculations the hull length used is $L_{boat} = 2.5$m, the span of the whole hull $B = 0.25$m, and its total depth beneath the undisturbed free surface is $T = 0.15625$m. Fig. 13 shows a sketch of the Wigley hull test case domain.

The domain is extremely similar to that used for the submerged spheroid. The numerical tank has dimensions $L_{\infty x} \times L_{\infty y} \times L_{\infty z}$. While the free surface boundary Γ_{fs} is located at $z = 0$. The hull is located at the center of Γ_{fs}.

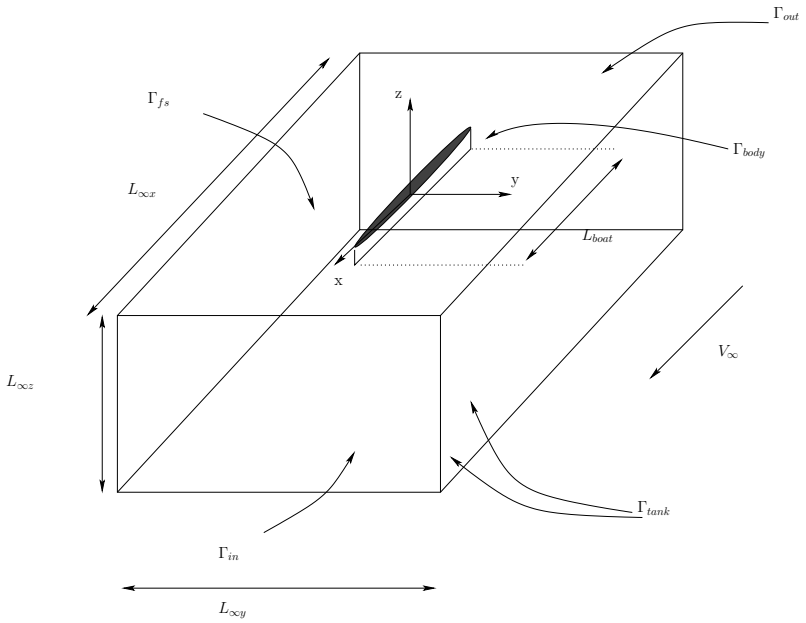

Figure 13: A sketch of the numerical domain. The wigley hull is placed in the center of the free surface. In the picture it is possible to see also the outer tank set with $L_{\infty x}, L_{\infty y}, L_{\infty z}$. The fluid enters from Γ_{in}, Γ_{tank} are the lateral surfaces and the bottom

This geometrical configuration coincides with that of a set of experiments performed at the university of Tokyo [16], which will be used as a benchmark in this test case. Six different velocities will be tested in order to compare them with the experimental results in [16] . The Froude number is defined again as

$$Fr = \frac{U_\infty}{\sqrt{gL_{boat}}} \tag{55}$$

4.2.1 Local refinement strategy and flow inspection

We have employed the same local refinement strategy already described in the submerged spheroid test case. On the boat, the grid is composed of 4 cells along the height of the hull, and 32 cells along its length. On the free surface, the mesh is set to be more refined around the hull and, to concentrate the degrees of freedom where the waves are expected to be.
We have computed the results using 5 local refinements on the free surface. We see the initial and final mesh for one of the cases considered in Fig. 14:

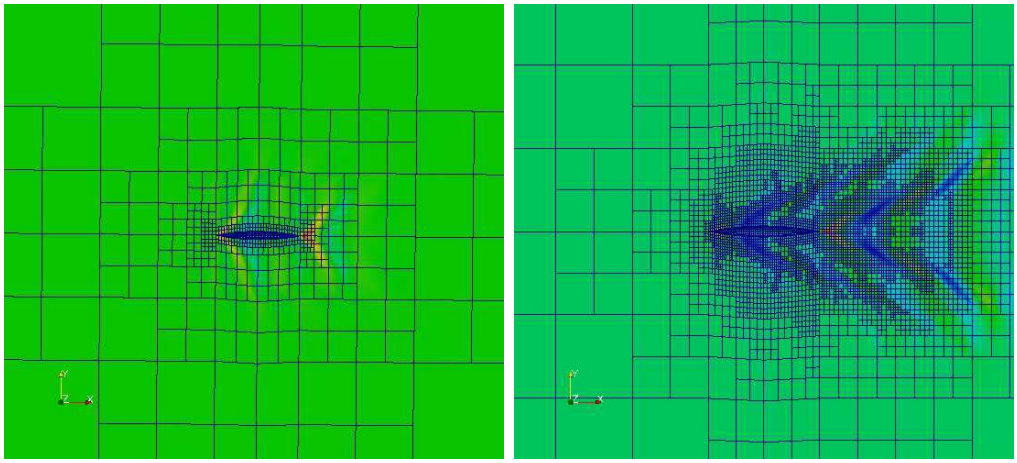

Figure 14: On the left, the free surface mesh at the initial level of refinement. On the right, the free surface mesh obtained after five refinement cycles

For the Wigley hull at two of the Froude numbers considered in the local refinement tests, we perform a qualitative comparison with the simple model described in [9].

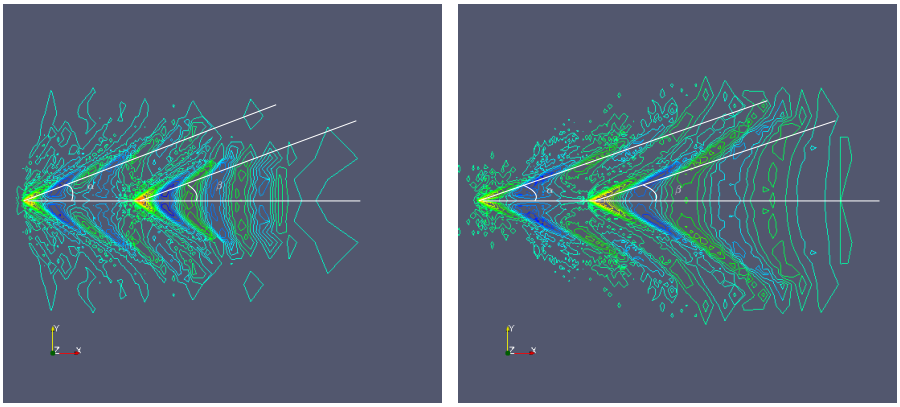

Figure 15: On the left, the Kelvin wave angle for $Fr = 0.267$ and on the right, the Kelvin wave angle for $Fr = 0.354$

Table 2: Kelvin angle for the Wigley hull

Fr	angle α	angle β
0.267	21	20
0.354	19	18

The two angles remain almost constant varying the Froude of the simulation. This fact agrees with what is reported in [9], and confirms that the present method is able to reproduce one of the most important feature of a Kelvin wake.

The local refinement strategy, since we are using an *a posteriori* error estimator, has a disadvantage in respect to what can be achieved using a prebuilt fixed mesh. This strategy needs to solve many linear system to refine the grid where the gradients of the unknowns are the highest. It also uses a large number of cell in its latest cycle. This situation increases the computational costs of the present method, the results of the local refinement strategy have been obtained in about 8 hours each. The major advantage is the possibility to concentrate the degrees of freedom only where the solution is more rapidly changing. This leads to better results.

Comparisons between the computed profiles on the hull surface, and corresponding experimental results of the University of Tokyo are now presented in Fig. 16

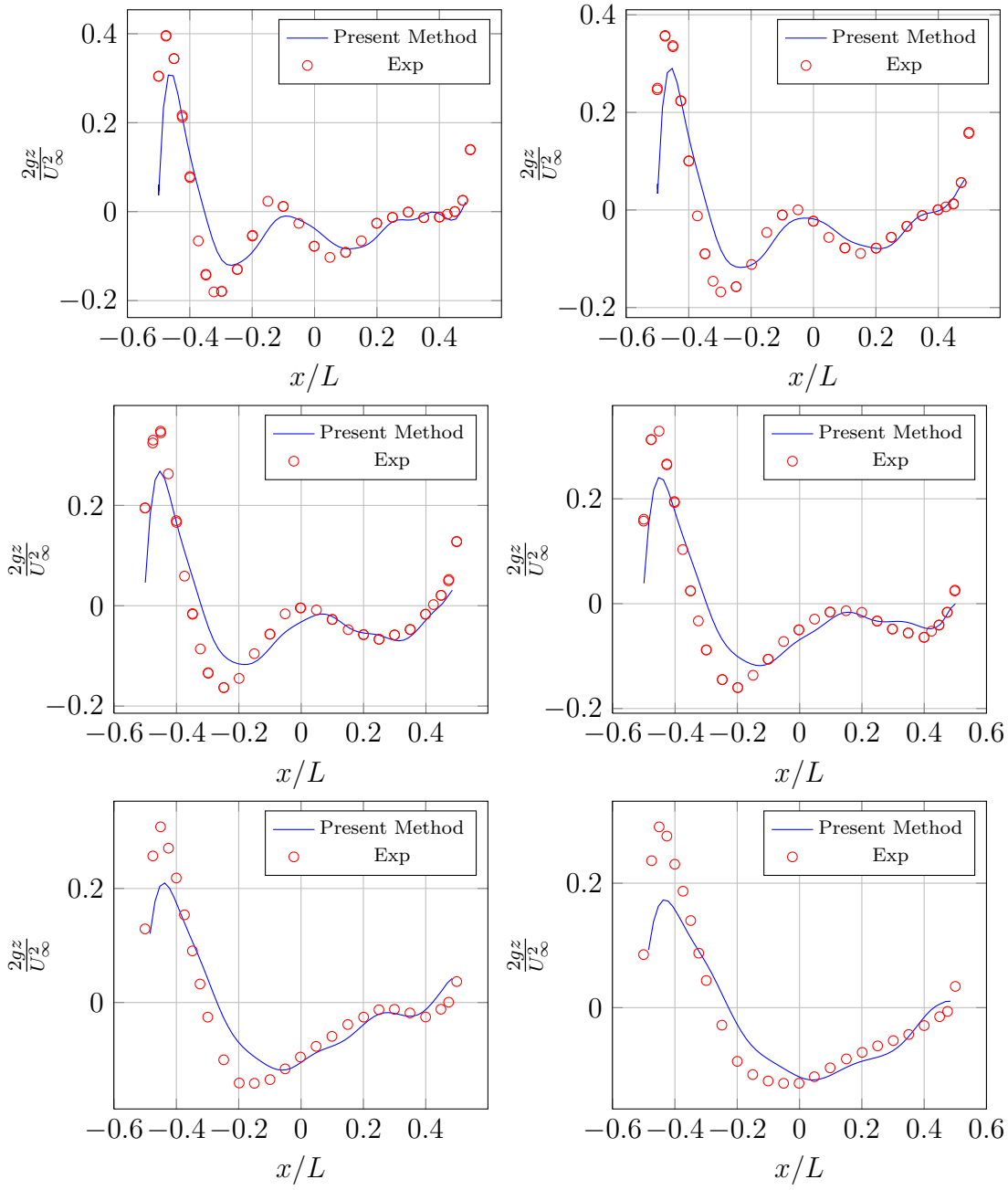

Figure 16: Non dimensional free surface elevation $2gz/U_\infty^2$ on the Wigley hull surface as a function of non dimensional longitudinal coordinate x/L, at different Froude numbers. The blue continuous line represents the result of the present method. The dots represent the university of Tokyo measurements [16]

The plots represent a comparison between experimental and computed wave heights along the hull, for $Fr = 0.250, 0.267, 0.289, 0.316, 0.354, 0.408$. In agreement with the experimental results the positive peaks on the hull are located just after the bow and near the stern. The plots suggest that, from a quantitative point of view, the model reproduces rather correctly the horizontal position of the peaks. Also the wavelength along the hull is correctly reproduced. As the Froude number increases the experimental water wave wavelength increases. The present method is able to reproduce such behavior too, as the location of the peaks remains quantitatively correct for all the Froude numbers considered. Despite this, the present model clearly underestimates the wave elevation. The problem is probably due to the choice of linearised free surface conditions. A linearised model is in fact not able to fully represent the wave generation process, as suggested in [23]. The results of Fig. 16 have been obtained using a linear continuous approximation for all the three unknowns ϕ, $\partial\phi/\partial x$ and $\partial\phi/\partial n$. For the last unknown a particular strategy was used to recover properly the derivative values on nodes belonging to both water and hull (see [11, 12]). Without such treatment, the computed solution results extremely inaccurate, since the normal derivative approximation is an average of the values on the boat and on the free surface, which are extremely different.

4.2.2 Comparison with other models

In this section we want to compare the results of our linearised potential model proposed with those obtained with different models. In the first case (see Fig. 17 on the left), we compare the present model solution with the established results of other linearised methods, [23]. In a second case (see Fig. 17 on the right), the present model will be compared to that obtained with an unsteady potential model with fully non linear free surface boundary conditions, presented in [18]. For both cases the test case considered is that of the Wigley Hull at $Fr = 0.316$.

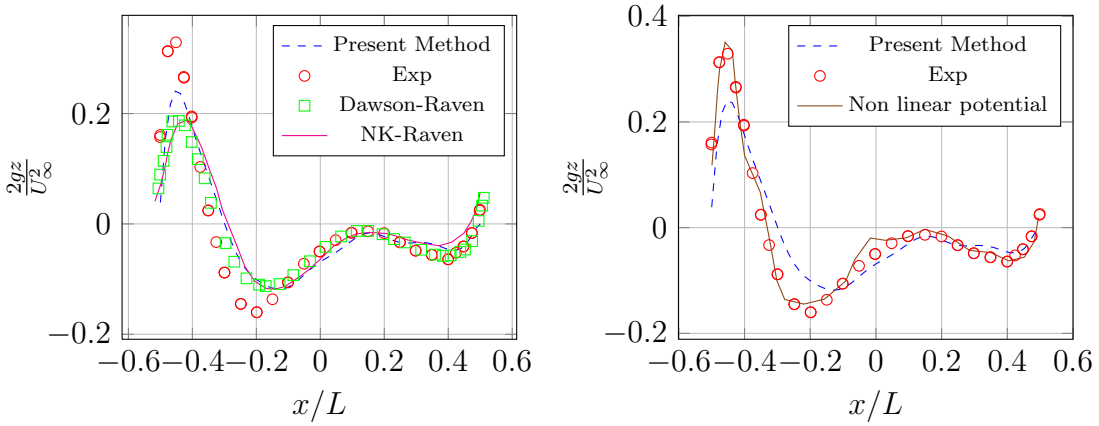

Figure 17: Non dimensional free surface elevation $2gz/U_\infty^2$ on the Wigley hull surface as a function of non dimensional longitudinal coordinate x/L, at Froude number 0.316. On the left we compare the developed method with other linearised models. The blue continuous line represents the waterline obtained in this work. The red dots represent the experimental results as reported by Ikemata *et alt.* in [16]. The green line represent the results of the Dawson method, [23]. The magenta line represents the result of the Neumann–Kelvin method, implemented in [23]. On the right we compare our method with a non linear BEM. The blue continuous line represents the waterline obtained with our BEM. The red dots represent the experimental results [16]. The brown line represents the result obtained using a non linear BEM presented in [18].

We first consider the plot showing the comparisonamong the wave profiles on the Wigley hull obtained with the linearised models. As we can see all the linearised methods considered underestimate the height of the peaks in the water profile on the hull. Thus, it was correct to speculate that the underestimation of wave elevation was mainly due to the choice of a linearised boundary condition on the free surface.

It is interesting to point out that the present model has less numerical dissipation than the other linearised strategies, as it employs the strongly consistent SUPG stabilisation method. As a result, we see that the wave crest is roughly 30% higher with respect to other linearised methods.

From the hull wave profile plot on the right, we can appreciate that the non linear potential model recovers the water elevations in a significantly more accurate fashion. This confirms one more time that the error of our method is mainly due to the free surface linearised model. Nonetheless we want to assess if the error can be further reduced by the choice of different boundary elements.

4.2.3 Quadratic BEM

Since we have proved the possibility of using a quadratic BEM in the submerged spheroid test case we now see its application on the Wigley hull.

In this case the free surface interacts directly with the body since it pierces the free surface. We remind that we are using an isoparametric BEM so we use the same quadratic approximation even for the geometry. This should increase the accuracy of the method because the hull has got a parabolic, therefore quadratic, formulation.

For this comparison we use $Fr = 0.316$ as we have already done in section 4.2.2.

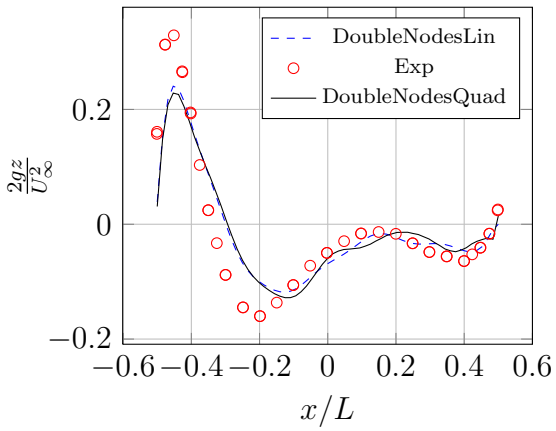

Figure 18: Non dimensional free surface elevation $2gz/U_\infty^2$ on the Wigley hull surface as a function of non dimensional longitudinal coordinate, at Froude number 0.316. The blue continuos line represents the waterline obtained with our linear BEM. The red dots represent the experimental results as reported in [16]. The black continuous line represents the waterline obtained with our quadratic BEM.

We have used a less refined mesh in the quadratic simulation. Thus the computational time is the same in both the simulation. We see that the two waterline almost overlap. Nevertheless the possibility of having non linear BEM approximation is very important. The calculation presented in the present paper state that the quadratic BEM is able to recover the well known results both for the submerged spheroid and the Wigley hull.

5 Conclusions

We have developed a mixed monolithic boundary element method to solve the Laplace equation coupled with a free surface boundary condition.

Following the idea presented in [10], our method relies on upwind projection techniques to recover the derivatives in the linearised boundary condition and suppress unphysical upstream waves. We employ surface finite element projections coupled with SUPG stabilisation techniques [2], to evaluate upwinded derivatives even on unstructured non conformal meshes. Using this kind of grids plays a key role in many of our simulations, where the solution gradients are concentrated in small regions surrounding the hull, and have a huge impact on the final computational cost of the simulations.

The proposed numerical model has been implemented into C++ applications which is based upon the OpenSOURCE library `deal.II`, [4, 3]. The numerical results obtained have been compared with available analytical and experimental results in naval literature, both on a fully submerged spheroid and on the Wigley hull. We have obtained reasonable agreement especially in the submerged spheroid case. On the Wigley hull we matched well established results of linearised methods, even though comparison with experiments plays in favour of fully non-linear models [18].

Our method can deal with boundary elements of arbitrary order, and with different approximation spaces for the flow potential and for its normal derivative. In the present work this capability is exploited in the most simple way. Both the flow potential and its normal derivative are approximated with a continuos functions, and sharp edges are treated as discussed in [11, 12]. We are currently exploring the application of mixed boundary element formulations on more elaborate models where, for example, the flow potential is treated using continuous finite element types, while its normal derivative is approximated using discontinuous Galerkin approximation, which would allow for a more natural treatment of sharp edges. In addiction we are studying the application of b-spline surface elements coupled with standard CAD data structures, without requiring a full iso-geometric framework in place, as done in [19].

Acknowledgements

This work was performed in the context of the projects OpenSHIP, “Simulazioni di fluidodinamica computazionale (CFD) di alta qualita per le previsioni di prestazioni idrodinamiche del sistema carena-elica in ambiente OpenSOURCE”, supported by Regione Autonoma FVG - POR FESR 2007-2013 Obiettivo competitivita regionale e occupazione, and of the project OpenViewSHIP, “Sviluppo di un ecosistema computazionale per la progettazione idrodinamica del sistema elica-carena”, supported by Regione Autonoma FVG - PAR FSC 2007-2013, Fondo per lo Sviluppo e la Coesione.

References

[1] M. Ainsworth and J. Oden. *A posteriori error estimation in finite element analysis*, volume 142. Hoepli, Mar. 1997.

[2] J. E. Akin. *Finite Element Analysis with Error Estimators*. Elsevier, 2005.

[3] W. Bangerth, R. Hartmann, and G. Kanschat. deal.II - a General Purpose Object Oriented Finite Element Library. *ACM Trans. Math. Softw.*, 33(4):24/1—-24/27, 2007.

[4] W. Bangerth, T. Heister, L. Heltai, G. Kanschat, M. Kronbichler, M. Maier, B. Turcksin, and T. D. Young. The deal.II Library, Version 8.1. *arXiv preprint arxiv:1312.2266v3*, Dec. 2013.

[5] K. A. Belibassakis, C. Feurer, T. P. Gerostathis, A. I. Ginnis, P. D. Kaklis, J. Karigiannis, K. V. Kostas, D. Mourkogiannis, C. G. Politis, and A. Theodoulides. A BEM-Isogeometric Method with Application to the Wavemaking Resistance Problem of Ship at Constant Speed. In *ASME 2011 30th Conference on Ocean, Offshore and Arctic Engineering*, 2011.

[6] C. A. Brebbia. *The Boundary Element Method for Engineers*. Pentech Press, 1978.

[7] X. Chen and G. X. Wu. On singular and highly oscillatory properties of the Green function for ship motions. *J. of Fluid Mech.*, 445:77–91, 2001.

[8] Z. M. Chen. Harmonic Function Expansion for Trans lating Green Functions and Dissipative Free Surface Waves. *Wave Motion*, 50(2):282–294, 2013.

[9] F. S. Crawford. Elementary derivation of the wake pattern of a boat. *Am. J. Phys.*, 52:782–785, 1984.

[10] C. W. Dawson. A practical computer method for solving ship-wave problems. In *Second International Conference on Numerical Ship Hydrodynamics*, pages 30–38, 1977.

[11] S. T. Grilli, P. Guyenne, and F. Dias. A fully non-linear model for three-dimensional overturning waves over an arbitrary bottom. *International Journal for Numerical Methods in Fluids*, 35:829–867, 2001.

[12] S. T. Grilli and I. A. Svendsen. Corner problems and global accuracy in the boundary element solution of nonlinear wave flows. *Engineering Analysis with Boundary Elements*, pages 178–195, 1990.

[13] S. Han Aydin. FEM-BEM Coupling for the MHD Pipe Flow in an Exterior Region. *Open Journal of Fluid Dynamics*, 3(3):184–190, 2013.

[14] T. H. Havelock. The Wave Resistance of a Spheroid. *Proceedings of the Royal Society*, pages 275–285, 1931.

[15] R. Hein, M. Duran, and J. C. Nedelec. Explicit Representation for the Infinite Depth Two Dimensional Free Surface Greens Function in Linear Water Wave Theory. *AIAN: Journal on Applied Mathematics*, 70(7):2353–2372, 2010.

[16] M.Ikehata, H.Tanaka, H.Adachi, M.Namimatsu, and S.Ogiwara. The summary of the cooperative experiment on Wigley parabolic model in Japan, 1983.

[17] A. Mola, L. Heltai, and A. Desimone. A stable semi-lagrangian potential method for the simulation of ship interaction with unsteady and nonlinear waves. In *17th International Conference on Ships and Shipping Research*, 2012.

[18] A. Mola, L. Heltai, and A. DeSimone. A stable and adaptive semi-Lagrangian potential model for unsteady and nonlinear ship-wave interactions. *Engineering Analysis with Boundary Elements*, 37(1):128–143, Jan. 2013.

[19] A. Mola, L. Heltai, and A. DeSimone. A fully nonlinear potential model for ship hydrodynamics directly interfaced with CAD data structures. In *24th International Ocean and Polar Engineering Conference*, 2014.

[20] J. N. Newman and J. M. Clarisse. Evaluation of the wave-resistence Green function near the singular axis. *J Ship Research*, 38, 2004.

[21] J. N. Newmann. *Marine Hydrodynamics*. the MIT Press, 1977.

[22] F. Noblesse, F. Huang, and C. Yang. The Neumann-Michell theory of ship waves . *J Eng Math*, 2012.

[23] H. C. Raven. *A Solution Method for the Nonlinear Ship Wave Resistance Problem*. PhD thesis, Technische Universiteit Delft, 1996.

[24] D. C. Scullen. *Accurate Computation of Steady Nonlinear Free-Surface Flows*. PhD thesis, University of Adelaide, 1998.

[25] K. Tanizawa. The state of the art on numerical wave tank. In *Proceeding of 4th Osaka Colloquium on Seakeeping Performance of Ships, Osaka*, pages 95–114, 2000.

[26] J. C. F. Telles. A Self-Adaptive Co-ordinate Transformation For Efficient Numerical Evaluation of General Boundary Element Integrals. *International Journal for Numerical Methods in Engineering*, 24:959–973, 1987.

[27] X. Wang, C. Liu, Z. Sun, M. Wu, and S. Zhang. Inherent Properties of Two Dimension Green Function with Linear Boundary Condition of Free Water Surface. *Applied Mathematics*, 4:97–99, 2013.

[28] X.-H. Wu, Z.-J. Chang, Y.-L. Lu, W.-Q. Tao, and S.-P. Shen. An analysis of the convectiondiffusion problems using meshless and meshbased methods. *Engineering Analysis with Boundary Elements*, 36:1040, 2012.

[29] R. W. Yeung. Numerical methods in free-furface flows. *Ann Rev. Fluid. Mech.*, pages 395–442, 1982.

MOX Technical Reports, last issues

Dipartimento di Matematica "F. Brioschi",
Politecnico di Milano, Via Bonardi 9 - 20133 Milano (Italy)

37/2014 Giuliani, N.; Mola, A.; Heltai, L.; Formaggia,L.
FEM SUPG stabilisation of mixed isoparametric BEMs: application to linearised free surface flows

36/2014 Abb,A.;Bonaventura,L.; Nini, M.;Restelli,M.;
Anisotropic dynamic models for Large Eddy Simulation of compressible flows with a high order DG method

35/2014 Tricerri, P.; Ded, L.; Deparis, S.; Quarteroni, A.; Robertson, A.M.; Sequeira, A.
Fluid-structure interaction simulations of cerebral arteries modeled by isotropic and anisotropic constitutive laws

34/2014 Antonietti, P.F.; Pacciarini, P.; Quarteroni, A.
A discontinuous Galerkin Reduced Basis Element method for elliptic problems

33/2014 Canuto, C.; Simoncini, V.; Verani, M.
Contraction and optimality properties of an adaptive Legendre-Galerkin method: the multi-dimensional case

32/2014 Agosti, A.; Formaggia, L.;Scotti, A.
Analysis of a model for precipitation and dissolution coupled with a Darcy flux

31/2014 Corno, J.; de Falco, C.; De Gersem, H.; Schps, S.
Isogeometric Simulation of Lorentz Detuning in Superconducting Accelerator Cavities

30/2014 Ferroni, A.; Formaggia, L.; Fumagalli, A.;
Numerical analysis of Darcy problem on surfaces

29/2014 Arioli, G.; Koch, H.
Some symmetric boundary value problems and non-symmetric solutions

Taffetani, M.; de Falco, C.; Penta, R.; Ambrosi, D.; Ciarletta, P.
Biomechanical modelling in nanomedicine: multiscale approaches and future challenges